INSTITUTE FOR DEFENSE ANALYSES

Assessment of Cloud Occurrence and Impact on Remote Sensing using Global, Open-source, Scientific Datasets (REDACTED)

A. J. Slawik, Principal Author

October 2016

IDA Document D-8175
(Redacted)
Log: H 16-001059
Copy

IDA *The Institute for Defense Analyses is a non-profit corporation that operates three federally funded research and development centers to provide objective analyses of national security issues, particularly those requiring scientific and technical expertise, and conduct related research on other national challenges.*

INSTITUTE FOR DEFENSE ANALYSES

IDA Document D-8175

Assessment of Cloud Occurrence and Impact on Remote Sensing using Global, Open-source, Scientific Datasets (REDACTED)

A. J. Slawik, Principal Author
E. A. Adelizzi
G. M. Koretsky

Executive Summary

This document discusses the prevalence of natural cloud blockages to remote intelligence, surveillance, and reconnaissance activities. The focus is on three case studies chosen to illustrate the value of open source global cloud coverage information. Our methodology and case study results are discussed with the strengths and weaknesses of the analysis highlighted.

The first case study was completed as part of a project for the Global Hawk Program Office. We delivered a detailed analysis of the Global Hawk's reconnaissance systems and capabilities compared with the U-2 spy plane [1]. We also explored the impact various viewing angles would have on cloud-free line of sight. Since the Global Hawk operates at a lower altitude than the U-2, this question directly concerned the comparative effectiveness of the platforms in remote intelligence, surveillance, and reconnaissance (ISR).

To estimate the probability of cloud-free line of sight as a function of viewing angle, we identified an open source dataset of global cloud coverage, CloudSat that provides vertical profiling of cloud layers. Using sets of geometrically gridded clouds, or snapshots of weather, at four separate geographical locations, we designed a line-of-sight algorithm to identify the frequency of cloud blockages. Our analysis found no substantial differences in the frequency of cloud-free line of sight for aircraft operating at the differing altitudes expected for the U-2 and Global Hawk platforms.

A second case study describes a cloud modeling addition to the IDA Sensing Effectiveness Evaluator (ISEE) [2]. Our cloud modeling feature is uses two-dimensional cloud grid information from NASA's MODIS CloudMask dataset. These grids specify in a nominally 1 by 1 km grid the location of clouds at a given instant on a particular day. This information is used in ISEE's line of sight calculation, with cloud presence implying full obscuration. Next, we using an ensemble of actual weather patterns and conducting many ISEE calculations, we obtain estimates of the degree to which clouds might hamper visual or infrared collection at given times and locations.

The third case study explores the local, spatial correlation of clouds. Analysis of the spatial correlation of clouds can answer a pertinent question for remote ISR: if it is cloudy in one region, how likely is it that a nearby location will also be blocked by clouds? Using an autocorrelation function applied to a dataset from MODIS's CloudMask product, the likelihood of concurrent cloudy regions over distance and direction was calculated in the Baltic region, in support of a study provided by IDA for the Office of Cost Assessment and Program Evaluation (CAPE), in the Office of the Secretary of Defense, on adversary ISR

systems. Cloud cover was found to be statistically similar on length scales of tens of kilometers, suggesting that geographically close targets will have approximately equal likelihood of being concurrently blocked by clouds – an intuitive finding that our analysis quantifies.

This document is intended to describe the research and analyses leveraged in these three separate studies and document the modeling techniques employed. In particular, this research emphasizes the value of free, easy to access, and peer-reviewed, scientific datasets of CloudSat, CALIOP, and MODIS. These datasets provide historical observations of cloud coverage, and more generally, the optical properties of the atmosphere on a global scale. Future studies regarding the effectiveness of remote intelligence gathering should draw upon the properties and variability of atmospheric conditions. As a brief characterization of the valuable sources of global cloud cover information, we list key features of the CloudSat, CALIOP, and MODIS datasets below.

Satellite Based Open-Source Scientific Datasets of Global Cloud Occurrence

Scientific Dataset	Summary	Resolution	Dates
CloudSat	Active radar, Nadir-only vertical profile of clouds	1 km along track 250 m vertical	2006-2011
CALIOP	Active lidar, Nadir-only vertical profile of clouds	333 m along track 30 m vertical	2006-2011
MODIS	Passive EO/IR, ± 55 FOV, planar view of clouds	250 m, 500 m, 1 km along and across track	2000-present

References

1. Institute for Defense Analyses, *Global Hawk Block 30 Improvements Study: Sensor Integration, Cost, and Effectiveness: Volume 1*, IDA Paper P-5236, 2015, UNCLASSIFIED.

2. Institute for Defense Analyses, *Development of the IDA Sensing Effectiveness Evaluator (ISEE) Model for Airborne Intelligence, Surveillance, and Reconnaissance*, IDA Paper P-4771, 2011, UNCLASSIFIED.

Contents

(This page is intentionally blank.)

1.   Introduction

Clouds cover about two-thirds of the earth's surface at any given time [1]. Considering that electro-optical and infrared (EO/IR) wavelengths cannot penetrate clouds, the prevalence of clouds in certain regions of the world warrants consideration when evaluating the effectiveness of long-range airborne and overhead surveillance and reconnaissance systems. In this report, we explore three separate case studies dealing with the effect of clouds on remote sensing. In all cases, historical weather information taken from scientific datasets is analyzed to determine statistics on clouds' spatial and temporal distributions for particular regions of the world. The frequency of cloud blockages as a function of viewing altitude, viewing angle, and season are analyzed. By measuring the historically observed frequency of cloud blockages, we estimate the potential difficulties airborne and overhead EO/IR sensors would have in achieving cloud-free line of sight with ground targets.

Historical observations provide insight into climate, but do not serve as a good prediction of weather (e.g., cloud cover at a specific location, date, and time of day). Here we are not considering the physical causes of clouds, but rather their frequency and morphology. The insights that these observations provide are useful to the U.S. defense community for long-term strategic planning and system evaluation. As a general example, EO/IR airborne sensors have been effective in recent years when monitoring objects on the ground in some of the drier regions of the world – e.g., the Middle East and portions of Central Asia. The Baltics and the Korean peninsula, as examples, have substantially cloudier climates, and the analysis presented in this report provides quantitative measures to predict and compare system performance in cloudy environments.

To provide context to this analysis, we first provide a general introduction to the effect of clouds on remote sensing (Chapter 2). The concept and calculation of the probability of cloud-free line of sight (PCFLOS) is discussed in Chapter 3. The scientific datasets used to estimate the frequency of cloud blockages in our case studies are introduced in Chapter 4, though additional resources for global cloud cover exist [1]. Chapter 5, the penultimate chapter, presents case studies, highlighting our methods and analysis.

The case studies discussed in this report reflect work that IDA performed for three separate studies. The first study was conducted for the Global Hawk Program Office, exploring the effect viewing angle has on visibility through clouds. We assessed historical data from Colorado State's CloudSat project and found that viewing angle generally has a marginal effect on visibility through the clouds (for the altitudes of interest in this study). The second study details the addition of a cloud model to the IDA Sensing Effectiveness Evaluator (ISEE) model. The new cloud model loads observations of clouds from the

National Aeronautical and Space Administration (NASA) Moderate Resolution Imaging Spectroradiometer (MODIS) instrument and incorporates this information into the ISEE simulation. The final study concerns statistics on cloud cover over the Baltic region of Europe, addressing the effectiveness of EO/IR sensors to image nearby locations concurrently. All three case studies utilize historical observations from global, open-source, scientific datasets.

Reference

1. Stubenrauch, C.J., W.B. Rossow, S. Kinne, S. Ackerman, G. Cesana, H. Chepfer, L. Di Girolamo, B. Getzewich, A. Guignard, A. Heidinger, et al., "Assessment of global cloud datasets from satellites: Project and database initiated by the GEWEX radiation panel," *Bulletin of the American Meteorological Society*, 94(7):1031–1049, 2013.

2.   The Effect of Clouds on Remote Sensing

A. Introduction to Radiative Transfer

To conceptualize the effect of cloud cover on remote sensing, consider an airborne (or space-borne) EO/IR sensor monitoring a target on the earth's surface. The surface of the earth, and any objects on it, both emit and reflect radiation. During daylight hours, the reflection of natural light via the sun's rays is the strongest source of radiation coming from an object; at night, radiative emissions in the infrared spectrum (often modeled as "blackbody" radiation) dominate. Ideally, the sensor's detector will be exposed to the emitted or reflected radiation and produce a coherent image that a human observer can interpret. A variety of physical and image processing factors are also important to this process.[1] This report focuses on the nature and frequency of natural cloud blockage and its effect on remote EO/IR sensing. To discuss this process quantitatively, we provide a brief introduction to the key concepts of radiative transfer.[2]

Two fundamental quantities of radiative transfer are intensity and flux density (often termed radiance and irradiance, respectively). Radiation transfers energy over time, area, a range of directions (treating light as a ray), and a certain range of wavelengths. If any one of those quantities is zero, no energy is transferred. Monochromatic intensity, I_λ, measures the transfer of energy via light per unit time, per unit area, for a specific direction, and for a specific wavelength. As monochromatic intensity is a function of the wavelength of light λ, integrating over a range of wavelengths yields the intensity I:

$$I = \int_{\lambda_1}^{\lambda_2} I_\lambda \mathrm{d}\lambda \tag{2-1}$$

The units of intensity are W m−2 sr−1, reflecting that power is transferred over an area and over a solid angle, measured relative to the unit area through which the power is being transferred. See Figure 2-1 for an illustration.

---

[1] See past work by IDA for details [1].

[2] The terminology of radiative transfer can be confusing or redundant and can differ from source to source; here we will use Qiang Fu's terminology in his chapter "Radiative Transfer" in *Atmospheric Science* [2].
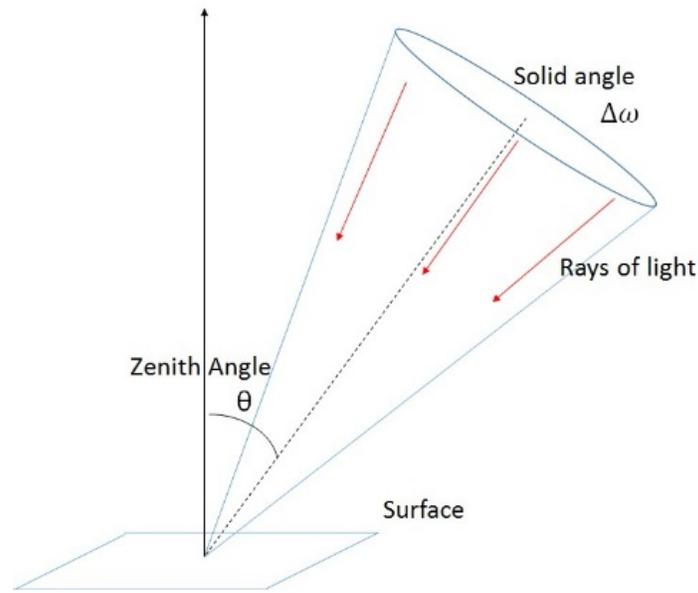
Figure 2-1. Radiance Measures Radiative Power along the Path of a Ray of Light, While Flux Density Sums All Rays Incident on a Surface for a Solid Angle

The monochromatic flux density F_λ measures the radiative transfer of energy per unit time at a specific wavelength through a unit area on a planar surface. Integrating the monochromatic intensity I_λ over a solid-angle hemisphere yields F_λ. Considering a planar surface, define a zenith angle θ as the angle off the normal to the surface. Assuming the radiation is incident on the surface from one direction, say above, the monochromatic flux density is

$$F_\lambda = \int_{2\pi} I_\lambda \cos\theta \, d\omega \tag{2-2}$$

where $d\omega$ denotes integration over solid angle, and the region of integration is 2π, or the full hemisphere above the surface. Figure 2-1 depicts the geometry over which flux density is defined, and its relationship to radiance or intensity. Similarly to radiance, integrating Eq. 2-2 over a range of wavelengths yields the flux density F:

$$F = \int_{\lambda_1}^{\lambda_2} F_\lambda d\lambda = \int_{2\pi} \int_{\lambda_1}^{\lambda_2} I_\lambda \, d\lambda d\omega \tag{2-3}$$

Finally, by considering a fixed area, A (such as the surface of the earth), the flux, E, or radiative power (measured in watts) incident upon a surface can be calculated:

$$E = \int_{\Delta A} \int_{2\pi} \int_{\lambda_1}^{\lambda_2} I_\lambda \, d\lambda d\omega dA \tag{2-4}$$

Returning for our conceptual airborne EO/IR sensor, the field of view of the sensor represents a solid angle that encompasses the target. The rays of light that are incident on the detector surface come from multiple sources. Figure 2-2 illustrates the various paths of light that are incident upon the detector of the sensor on an airborne platform (see figure for explanation).
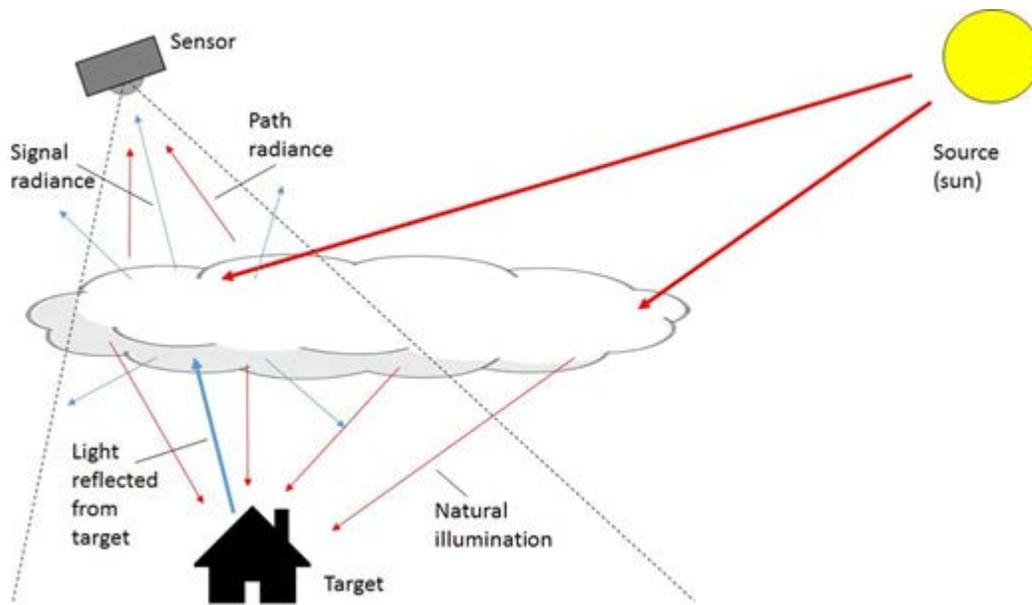
Figure 2-2. Diagram Depicting the Role Clouds Play in Remote Sensing During the Day

A sensor is directed to a target, such that the target lies within its field of view (dashed black line). The sun's rays (red arrows) hit the cloud and scatter light in all directions, illuminating the target on the ground in natural light. The illuminated target reflects this radiation (blue arrows). The cloud attenuates this signal coming from the target by scattering the light in other directions as well as via frequency-dependent absorption. In addition to this reduction in signal, path radiation from the sun is scattered by the cloud into the sensor's field of view, cluttering the signal with noise and making the cloud opaque.

The extinction of an electromagnetic wave (in our case, a visual signal emanating from a target or target area) occurs through the processes of scattering and absorption. The liquid droplets and solid ice particles that compose clouds will scatter, and to a lesser extent absorb, electromagnetic radiation in the visible and infrared spectrum. The scattering of a signal by a cloud of droplets is elastic; the frequency of the light remains the same, but its direction changes. The probability that a photon will pass through a typical cloud obstruction without scattering at least once is very low, and thus an EO/IR signal passing through a cloud will lose its coherence.

The processes of scattering and absorption by particles are idealized to be linear with respect to three quantities: the intensity I_λ, the local concentration of the particles, and the "effectiveness" of scattering and absorption for each particle [2]. This implies that doubling the intensity doubles the amount of light scattered or absorbed, with similar dependence on concentration and effectiveness. Consider an individual ray of light passing through an infinitesimally thin layer of a cloud of particles. First, assuming that each particle is identical, the monochromatic intensity will decrease an amount dI_λ by passing a distance ds through the cloud according to,

$$dI_\lambda = -I_\lambda K_\lambda N\sigma ds \qquad (2\text{-}5)$$

where K_λ is the efficiency or "effectiveness" of either scattering or absorption, N is the number of particles per unit volume, and σ is the cross-section of each identical particle. Thus, the total extinction of a ray of light through a cloud is the sum of the contribution

from each particle. Likewise, the contribution from different particle types are additive, and the efficiency of scattering and absorption can be treated as separate, additive terms. Assuming a set of J total particle types, the extinction of light through the thin layer is expressed as,

$$dI_\lambda = -I_\lambda\left(\sum_{j=1}^{J} K_{\lambda,j,\text{scattering}}N_j\sigma_j + \sum_{j=1}^{J} K_{\lambda,j,\text{absorption}}N_j\sigma_j\right)ds \qquad (2\text{-}6)$$

where $K_{\lambda,j,\text{scattering}}$ represents the efficiency of scattering for the jth particle type and $K_{\lambda,j,\text{absorption}}$ represents the efficiency of absorption. Define the quantity $\alpha_\lambda = K_\lambda N\sigma$ as the scattering or absorption coefficient.

Equations 2-5 and 2-6 measure extinction (absorption plus scattering) over an infinitesimal path length ds. We can now define the optical depth of a cloud of particles. For simplicity, consider a ray of light passing a length L through a cloud of identical particles that only scatter light. Define $I_{\lambda,0}$ as the monochromatic intensity of light incident on the cloud, and $I_{\lambda,L}$ the monochromatic intensity leaving the cloud. Integrating Eq. 2-5 over the path yields Beer's law:

$$\frac{I_{\lambda,L}}{I_{\lambda,0}} = e^{\left(-\int_0^L \alpha_\lambda(s)ds\right)} \qquad (2\text{-}7)$$

This quantity is termed the transmissivity of the cloud. Another useful measure of a cloud, or a vertical slab of the atmosphere, is the optical depth τ_λ:

$$\tau_\lambda = \int_0^L \alpha_\lambda(s)\, ds \qquad (2\text{-}8)$$

While τ is unitless, it is dependent on the path through the cloud. If the cloud is homogeneous, the attenuation coefficient is constant and $\tau = \alpha L$. Notice that the attenuation coefficient has units of 1/length and is thus independent of the dimensions of the depth L of the cloud. The inverse of the attenuation coefficient is $l = 1/\alpha$, the mean free path of a photon in the cloud. The mean free path can be thought of as the average (or expected) distance traveled by a photon before a scattering or absorption event occurs.

Although from the standpoint of remote sensing a photon emitted from a target will be "lost" from a signal due to scattering, a portion of light from the ground may still escape through the cloud and be detected by the sensor (consider the diagram in Figure 2-2). On a very cloudy afternoon, a significant portion of the sun's rays still diffuse through the clouds via scattering. However, the sun's location is not visible from the ground, since after multiple scattering events, the light is diffusely scattered among the cloud deck. Visible and infrared light traveling through clouds typically scatters multiple times; thin clouds in which single scattering dominates produce dramatic optical effects such as glories and the sun's corona.

Electro-optical and infrared sensors are incapable of acquiring a target through an even moderate cloud obstruction. The attenuation coefficient of low to middle height clouds (cumulus, stratus, and nimbostratus type clouds) ranges from 100 to 500 dB/km for wavelengths of 0.4-10 μm [3]. This corresponds to over 99.9-percent loss per km, and

EO/IR systems operating in this range will suffer a near complete loss of signal from cloud obstruction. Higher, ice-phase cirrus-type clouds are less optically thick and can be very difficult to detect [4]. The combined active radar systems CALIPSO and CloudSat (discussed in Section 4.1) have a detection sensitivity of optical depth in the visible range greater than about 0.1 for ice clouds, and clouds with a lower depth may be missed [5]. A recent scientific survey by the Global Energy and Water Cycle Experiment Radiation Panel of satellite based sources of global cloud cover uses a visible optical depth threshold of 0.1 to define the "global total cloud amount" corresponding to at least a 9.9-percent loss of signal through the cloud [6]. In the case studies presented in Chapter 5, we use this common detection threshold to define a cloud. The typical cloud, defined colloquially, far exceeds this detection threshold.

Returning to our conceptual airborne EO/IR sensor, clouds obstruct remote information extraction by increasing the amount of light detected by the sensor not associated with the target and by attenuating the signal from the target. Scattering of ambient light into the sensor by clouds is a three-dimensional (3D) problem and cannot be modeled by the attenuation coefficient of clouds alone. To determine the spatial distribution of scattered photons traveling through a mass of clouds, a more sophisticated treatment of light-matter interactions is necessary. The next section briefly discusses a more rigorous treatment of cloud's effect on remote sensing.

B.   Scattering of Light by Liquid Cloud Droplets

Clouds are composed of liquid or solid water particles on the scale of microns to tens of microns. These particles are distributed quasi-randomly in a cloud, with significant variability in density possible [7, 8]. The optical properties of a cloud of droplets are different from the optical properties of contiguous liquid water. The fundamental reason for this is the small size of the droplets. The visible and near-infrared band ranges from wavelengths of 400 nm to about 2 µm: the same order of size as the cloud particles. In this regime, the wave nature of light becomes significant and the physics of light-matter interactions is best described by Maxwell's equations.[3]

Consider an electromagnetic wave incident on a droplet of water. By treating the incident wave as a ray, we can use Fresnel's equations to calculate the reflected and refracted rays of light through the particle. This simple approach reasonably models the optical patterns of rainbows [2, 9], which are caused by large rainwater droplets about 1 mm in diameter. However, for common cloud droplets on the micron scale, the incident electromagnetic wave produces a pronounced diffraction pattern that is not modeled using rays. Mie theory approaches this problem using Maxwell's equations. Using a generating scalar function, the coupled, vector equations of Maxwell can be converted into an eigenvalue problem with a series solution [10]. The scattering patterns of the incident wave

---

[3]   For a great overview of the physics of light scattering by small particles, see section 4.4 of Wallace and Hobbs' book *Atmospheric Science* [2].

can thus be approximated using a sufficient number of terms of this series solution. Evaluating the resulting expressions for the scattered waves is not analytically tractable and requires numerical analysis.

The total cross section σ of a particle roughly captures how much it obstructs an incident wave (see Eq. 2-5). For particles much larger than the wavelength of light (such as a baseball on a sunny day), the total cross section of the particle is simply its geometric cross-section σ_{geo}: the area of the particle projected onto the plane perpendicular to the light. Spherical droplets of water primarily scatter light, so the total cross-section of a droplet is equivalent to its scattering cross-section σ_{sca}. Due to diffraction, the scattering cross-section of a spherical droplet is approximately a factor of two larger than its geometric cross-section! In other words, the droplet obstructs the light greater than its size would indicate. As a further complication, the scattering cross-section sensitively and non-monotonically depends upon the size of the droplet.

A conceptually useful approximation to the Mie-theory solution is presented by van de Hulst in his 1957 book *Light Scattering by Small Particles* [11]. Defining the efficiency factor Q_{ext} as the ratio of the scattering cross-section to the geometric cross-section, the efficiency factor for a water droplet can be approximated as,

$$Q_{ext} \approx 2 - \frac{4}{p}\sin p + \frac{4}{p^2}(1 - \cos p) \tag{2-9}$$

where $p = 4\pi r(m - 1)/\lambda$, with r being the radius of the spherical droplet; $m = 1.33$, the index of refraction for water; and λ is the wavelength of the light. Figure 2-3 plots the efficiency factor for multiple sizes of droplets as a function of wavelength. Note that the curves appear to oscillate about a value of 2, indicating that the scattering cross-section of the droplet is twice as large as its geometric cross-section. Although the approximation captures the general behavior of Q_{ext}'s dependence on wavelength and droplet radius, the exact Mie solution is significantly more complicated.[4]

The distribution of scattering angles resulting from light incident upon a single droplet are similarly dependent upon droplet radius and the light's wavelength. However, a general characteristic remains the same: the scattering angle is forward peaked, meaning that a scattering event is more likely to slightly deflect the trajectory, rather than reflect. The differential cross-section in the backscattering region is about three orders of magnitude lower than the forward-scattering cross-section [13]. As mentioned in the previous section, any scattering event effectively blurs a target by weakening the signal and increasing noise, and as such the scattering angle is less important than the scattering cross-section.

---

[4] See page 105 in Bohren [10], and page 177 in van de Hulst [11] for a complete derivation of the exact Mie solution, and for a nice overview, see Refs. 2 and 12.
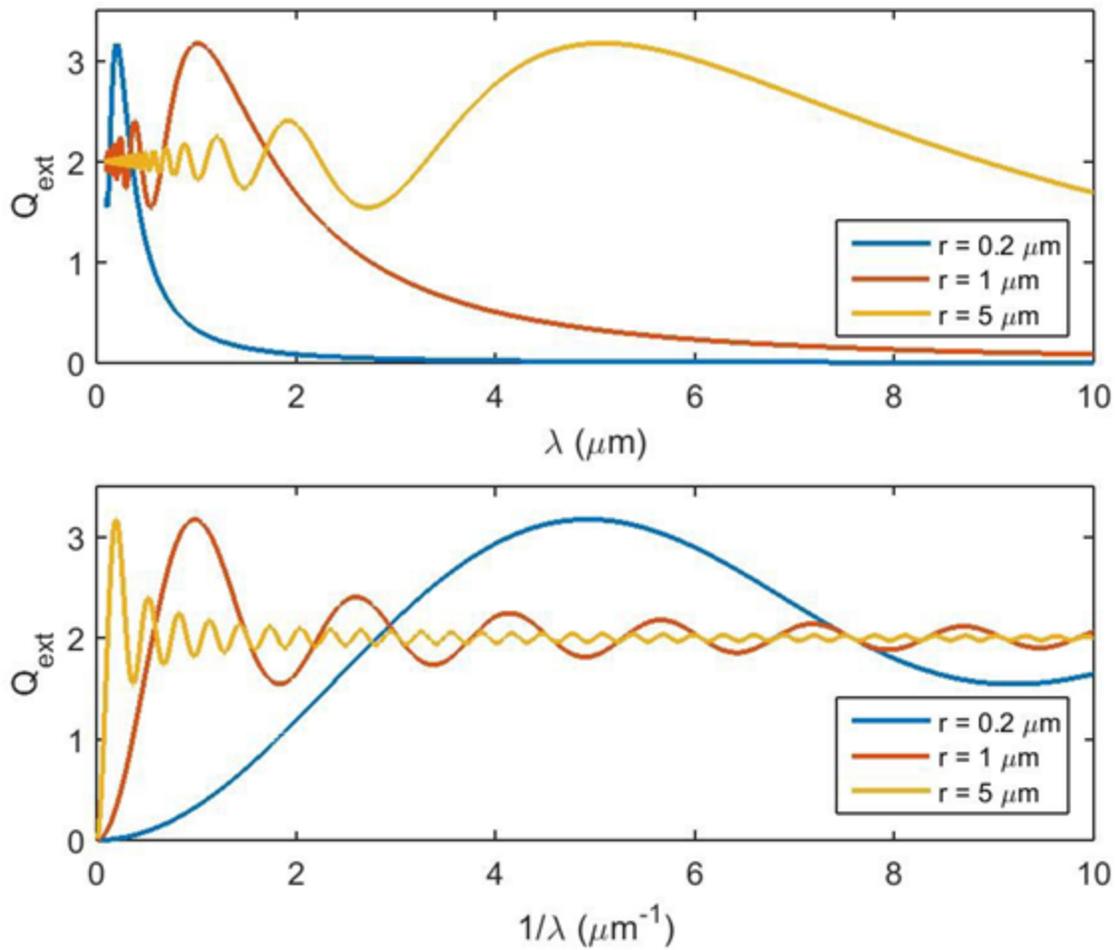
Figure 2-3. Approximate Efficiency Factor vs. Wavelength (Top Panel) and Inverse Wavelength (Bottom Panel) for Water Droplets with Three Separate Radii

Efficiency factor is the ratio of scattering cross-section to geometric cross-section. Low- and mid-altitude water clouds typically have droplets with radii from 1 to 50 μm. Notice the sensitive dependence of the scattering cross-section on droplet radius and wavelength.

Clouds are not monodisperse; a parcel of cloud mass will contain a distribution of droplet sizes. Given a particular distribution, and assuming that the particles are randomly distributed and separated from each other by average distances larger than their radii, the scattering cross-section of the cloud mass is the same as the summation of each individual droplet's scattering cross-section [12]. Integrating the scattering cross-section over the frequency distribution of cloud droplets along a path defines the scattering cross-section per unit volume $\beta_{\lambda,\text{sca}}$:

$$\beta_{\lambda,\text{sca}} = \int_0^\infty \sigma_{\lambda,\text{sca}}(r)n(r)\, dr \tag{2-10}$$

where $\sigma_{\lambda,\text{sca}}(r)$ is the scattering cross-section at wavelength λ of a single particle of radius r and $n(r)$ is the distribution function of the particle size per unit volume. The scattering cross-section per unit volume has units of inverse length, can vary along the extent of the cloud, and is an analogous measure to the material attenuation coefficient α_λ presented in Eq. 2-8. The cross-section per unit volume can be related to the optical depth of the cloud directly:

$$\tau = \int_0^L \beta_{\text{sca}}(z)\, dz \qquad (2\text{-}11)$$

where L is the spatial extent of the cloud along the z axis. Using a distribution of cloud droplets $n(r)$ and a cloud geometric thickness L, Equations 2-9 through 2-11 provide an estimate of the extinction of a signal through the cloud as a function of wavelength. Integrating over wavelength, as in Eq. 2-1, for a particular source spectrum, such as the sun, yields the total attenuation of the signal.

Ice crystals in clouds are generally not spherical and can assume a variety of shapes. Commonly they are characterized as flat plates or thin rods [7]. Regardless of shape, ice crystals primarily scatter radiation, and their optical properties can be crudely treated in an analogous fashion to spherical droplets.[5]

C.   Typical Spatial Distributions of Clouds

Clouds range in size from hundreds of meters to hundreds of kilometers. Large storm fronts can dominate a landscape, and fair weather cumulus clouds can dot the sky, casting shadows intermittently on a windy afternoon. The simplest division of clouds into cumulus type and stratus type is based upon this contrast of isolated clouds existing in small, discrete chunks and roughly uniform planes with great horizontal extent. It is this spatial (and spatiotemporal) heterogeneity that make the optical properties of clouds difficult to quantify and generalize, particularly with regards to the radiation budget of the earth's atmosphere [14]. However, because of the interest in clouds' role in climate change, the statistics of clouds' spatial distributions have recently been well studied.

The earliest comprehensive satellite studies on the horizontal extent of clouds determined that cloud cover has sizable contributions from the smallest measured scales to the largest.[6] The distribution of cloud sizes, either measured as an area or a length, has been found to reasonably follow a power law with a negative slope [15-17]. Defining a number density function $n(x)$ such that $n(x)dx$ is the number of clouds with sizes between x and $x + dx$, consider the power-law,

$$n(x) = ax^{-\beta} \qquad (2\text{-}12)$$

where α and β are constants. The magnitude of β determines the relative contribution large clouds make to total cloud cover. With a β of 2, each logarithmic interval (say 1-10 meters, 10-100 meters, etc.) contributes the same amount to total cloud coverage. For smaller β, larger clouds begin to increasingly dominate, and all systematic cloud studies have found β to be less than 2. A particular parcel of cloud will thus tend to belong to a large cloud mass on the order of hundreds of kilometers in scale, and, as such, clouds of these scales

---

[5]   See Chapters 2 and 8 of Wang's *Clouds and Precipitation* [7] and Volume 2 of the *Infrared and Electro-Optical Systems Handbook* [12] for details.

[6]   This paragraph summarizes the summary of recent work on measuring clouds' horizontal distributions provided by Robert Wood et al. [15].

form the bulk of cloud cover. Using MODIS's CloudMask dataset, discussed in Section 4.B, $\beta \approx 1.67$ over the globe, excluding the polar regions [15]. Curiously, this satellite-based result is in reasonable agreement to those using aircraft-based datasets, even of particular cloud types, such as cirrus or stratocumulus. Most critically to the case studies presented in this work, the fitted power law matches observations well down to the smallest scales measurable, about 150 meters for airplane observations and about 1 km for the satellite observations. Using the best fit power-law, we expect that about 5 percent of total cloud cover is composed of clouds with lengths less than 1 km [15]. Thus, we can be confident that resolving clouds to horizontal resolutions of 1 km will capture the majority of cloud cover, and clouds on smaller scales may still be captured in the datasets depending upon their optical thickness.

References

1. Institute for Defense Analyses, *Visual and Infrared Predictor (VIP) Derivations*, IDA Paper D-5397, 2015, UNCLASSIFIED.

2. Wallace, J.M. and P.V. Hobbs, *Atmospheric science: an introductory survey*, volume 92, Academic Press, 2006.

3. RAND, Chen, C.C., Attenuation of Electromagnetic Radiation by Haze, Fog, Clouds, and Rain, R-1 694-PR, 1975.

4. Mace, G.G., Y. Zhang, S. Platnick, M.D. King, P. Minnis, and P. Yang, "Evaluation of cirrus cloud properties derived from MODIS data using cloud properties derived from ground-based observations collected at the ARM SGP site," *Journal of Applied Meteorology*, 44(2):221–240, 2005.

5. Stephens, G.L., D.G. Vane, R.J. Boain, G.G. Mace, K. Sassen, Z. Wang, A.J. Illingworth, E.J. O'Connor, W.B. Rossow, S.L. Durden, et al, "The CloudSat mission and the A-Train: A new dimension of space-based observations of clouds and precipitation," *Bulletin of the American Meteorological Society*, 83(12):1771–1790, 2002.

6. Stubenrauch, C.J., W.B. Rossow, S. Kinne, S. Ackerman, G. Cesana, H. Chepfer, L. Di Girolamo, B. Getzewich, A. Guignard, A. Heidinger, et al., "Assessment of global cloud datasets from satellites: Project and database initiated by the GEWEX radiation panel," *Bulletin of the American Meteorological Society*, 94(7):1031–1049, 2013.

7. Wang, Pao, *Physics and dynamics of clouds and precipitation*, Cambridge: Cambridge University Press, 2013.

8. Beals, M.J., J.P. Fugal, R.A. Shaw, J. Lu, S.M. Spuler, and J.L. Stith, "Holographic measurements of inhomogeneous cloud mixing at the centimeter scale" *Science*, 350(6256):87–90, 2015.

9. Cowley, Les, "Water Droplets," accessed: 2016-04-5.

10. Bohren, Craig F. and Donald R Huffman. *Absorption and scattering of light by small particles*. John Wiley and Sons Inc., 1983.

11. Van de Hulst, Hendrik C., *Light Scattering by Small Particles*. New York: John Wiley and Sons Inc., 1957.

12. Smith, F. G., J. S. Accetta, and D. L. Shumaker, eds., *The Infrared & Electro-Optical Systems Handbook*; Volume 2, *Atmospheric Propagation of Radiation*, Smith, F. G., ed., Ann Arbor, MI: Infrared Information Analysis Center Environmental Research Institute of Michigan and Bellingham, WA: SPIE Optical Engineering Press, 1993.

13. Glasstone, Samuel and Philip J. Dolan, eds., *The Effects of Nuclear Weapons*, Washington, DC: Government Printing Office, United States Department of Defense and the Energy Research and Development Administration.

14. Rossow, W. B., C. Delo, and B. Cairns, "Implications of the observed mesoscale variations of clouds for the earth's radiation budget" *Journal of Climate*, 15(6):557–585, 2002.

15. Wood, R. and P. R. Field, "The distribution of cloud horizontal sizes" *Journal of Climate*, 24(18):4800–4816, 2011.

16. Leahy, L.V., R. Wood, R.J. Charlson, C.A. Hostetler, R.R. Rogers, M.A. Vaughan, and D.M. Winker, "On the nature and extent of optically thin marine low clouds," *Journal of Geophysical Research: Atmospheres*, 117(D22), 2012.

17. Trebbin, Nico, "Cloud Statistics from Calipso Lidar Data for the Performance Assessment of a Methane Space Lidar," (PhD diss., TU München, 2013).

3.   The Probability of Cloud-Free Line Of Sight (PCFLOS) Metric

A. Overview

A powerful and intuitive measure of the effect of clouds on sensors is the PCFLOS, which measures the probability that a line of sight between an observer and a target is not obstructed by clouds. For a single observation of a single target at a specific time, the determination of whether or not a cloud is in the way (CFLOS) is unambiguous and deterministic. Since the task of deterministically calculating where and when clouds will occur in the future, even given perfect information in the present, is an impractical task (and not expected to be possible as turbulence models are chaotic), we must rely upon a probabilistic measure for predictions. As any casual observer of weather forecasting knows, numerical weather prediction models used for operational forecasting can provide accurate predictions at best a week in advance, and these predictions have uncertainties associated with them.

The PCFLOS metric is used not only in the surveillance and reconnaissance community for strategic assessment [1-5], but also in the academic community for calculations of the earth's radiation budget [6-8]. Global climate studies require high-fidelity cloud modeling, and the sensitive dependence of clouds' radiative properties on local and global heterogeneity has a significant effect on the earth's radiation budget. As such, theoretical and experimental work has gone into defining and approximating PCFLOS on both a global scale and for particular cloudy scenes (e.g., cumulus clouds). Here we will consider PCFLOS as a practical metric, more familiar to the reconnaissance community.

The probability of cloud-free line of sight uses past observations to make predictions. PCFLOS should be defined by three elements: location of target, location of observer, and times of observation. For example, given a set of N observations of a particular target under ideally the same conditions, we can estimate the PCFLOS as simply the number of observations with cloud-free line of sight over the total number of observations N:

$$\text{PCFLOS} = \sum_{i=1}^{N} {\text{CFLOS}_i}/{N} \qquad (3\text{-}1)$$

Here the measure CFLOS is taken to be zero given a cloud blockage and one given cloud-free line of sight.

Interpreting CFLOS as a random variable, Eq. 3-1 is the estimator for the expected value of CFLOS. Thus, the sampling of the distribution of CFLOS should be under similar conditions to that of the PCFLOS metric one is trying to estimate. (Obviously, observing

clouds out a window does not effectively estimate the occurrence of clouds in the Sahara desert). Ideally, the set of N observations would be independent, in that the probability that one observation is cloud-free does not affect the probability of another observation being cloud-free. In practice, no two observations are completely independent, but this assumption of independence becomes more valid the further apart in time observations are taken.

The probability of cloud-free line of sight as presented in this report assumes an observation is practically instantaneous and scheduled independent of cloud cover. Obviously, an observer who only attempts to make observations in times of clear weather will achieve more instances of clear line of sight with the target. In this situation, to achieve an appropriate estimate for PCFLOS, the set of observations N should reflect the scenario one is trying to estimate. In addition, if the observer is willing to maintain a constant observation of a target until the clouds break, likewise, the set of observations N should reflect this scenario. PCFLOS can be generalized to measure whether or not the target is visible for at least a fixed amount of time, but the metric becomes more difficult to calculate and rather intractable. The analysis presented in the third case study of this report begins to address this question, providing a metric for the chance of simultaneously tracking multiple targets in close proximity to each other (see Section 5.C).

The PCFLOS metric greatly simplifies the more complicated treatment of radiation transport discussed in Chapter 2. At first glance, the treatment of clouds as either being present or not present appears incapable of capturing the complicated physical phenomena of cloud blockages to remote sensing. For instance, translucent cloud edges, thin fog-like stratus cover, and wispy high clouds can partially obstruct an object in the visible and infrared spectrum. While acknowledging the existence of these "gray areas," the typical cloud blockage completely obscures a target (see Section 2.C). In addition, once a detection threshold is defined, say a visual optical depth of $\tau > 0.1$, the presence of clouds can be determined unambiguously. Thus the PCFLOS metric provides a straightforward and useful assessment on the frequency of cloud blockages.

B. Estimating PCFLOS and the 3D Cloud Effect

To construct an estimate for the PCFLOS at a particular target, one can use a set of observations of particular instances of weather. A spatial distribution of clouds in a grid represents a single observation. By placing imaginary observers and targets in this cloudy field, it becomes a straightforward question whether or not a cloud-free line of sight exists. Cycling through many instances of weather provides statistics of this measure. A common shortcut to extract more information out of a single cloudy scene is to assume local spatial correlation is equivalent to short-term time correlation: the clouds one observes at a particular location are just as likely to have been observed a short distance away. To illustrate this concept, consider Figure 3-1.
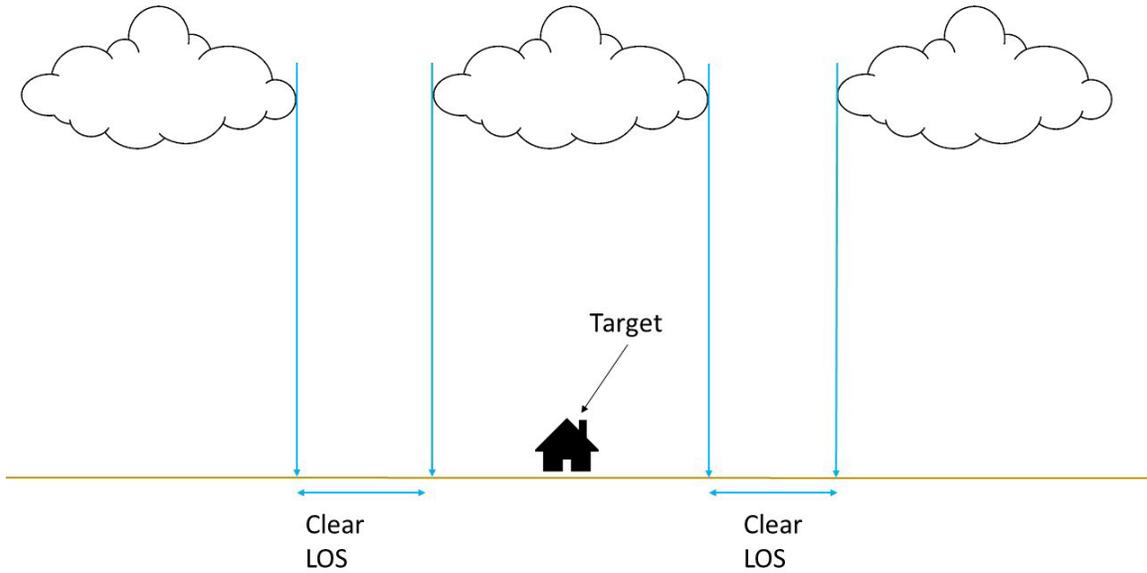
Figure 3-1. Schematic of Clouds Obstructing a Scene in Two Dimensions

The target is not visible directly overhead. PCFLOS in this scene can be estimated as one minus the fractional area covered in clouds.

Figure 3-1 depicts a two-dimensional scene of a partially cloudy field over a single target, a house. When viewed from above, the house is completely obscured. However, one might imagine that after a few minutes, the clouds would drift and the house would become visible from above. If the observation is made independent of cloud cover, the clouds as they appear are just as likely to be displaced a small amount. To extract as much information as possible from this particular scene, one can estimate PCFLOS in the particular cloudy field. Picking an area of the ground, say a 1 km × 1 km block, the amount of area visible divided by the total area provides an estimate of PCFLOS at the scene:

$$\text{PCFLOS}_{\text{scene}} = \frac{A_{\text{clear}}}{A_{\text{total}}} = 1 - \frac{A_{\text{cloudy}}}{A_{\text{total}}} = 1 - \text{CF} \tag{3-2}$$

where CF is the cloud fraction, or fraction of ground covered in clouds.

Equation 3-2 implies a slightly more complicated interpretation of PCFLOS than a simple, frequentist interpretation of Eq. 3-1. Given a set of N cloudy scenes, the PCFLOS at the target can be approximated as,

$$\text{PCFLOS} = \sum_{i=1}^{N} \left.(1 - \text{CF}_i)\middle/ N\right. = \sum_{i=1}^{N} \left.\text{PCFLOS}_i\middle/ N\right. \tag{3-3}$$

or simply the mean of the PCFLOS over all scenes or instances of weather. The formula is reasonable as long as the area from which the cloud fraction is calculated is relatively small, i.e., the weather is on average the same. In our third case study presented in this report, the annual cloud cover is calculated over the Baltic region for a 1 km × 1 km grid using 4 years of data. As expected, the annual cloud cover is approximately constant over small length scales, with some exceptions (see Section 5.C).

Realistically, weather patterns will vary by day, season, and year. Yearly variations in global climate are beyond the scope of this report; in the proceeding case studies, we

3-3

take the seasonal weather patterns observed in recent years as characteristic of seasonal weather patterns in the near future. Of interest to the field of remote sensing is PCFLOS of a ground target as a function of location, season, altitude, and viewing angle. The global spatial and seasonal variability of cloud cover is a well-studied phenomenon, and satellite-based cloud datasets typically provide averaged cloud cover [9]. If an observer attempts to make observations directly above a target independent of the weather, these averages provide a reasonable approximation to the observer's PCFLOS.

Global climate studies require high-fidelity cloud modeling, and the sensitive dependence of clouds' radiative properties on viewing angle has a significant effect on the earth's radiation budget. In the words of Yingtau Ma, "for low or middle clouds a cloud fraction change of no more than 5 percent would generate an error in the surface longwave CF (cloud forcing) of the same magnitude as the direct forcing from CO_2 doubling" [6]. As such, theoretical and experimental work has gone into defining and approximating PCFLOS as a function of viewing angle on both a global scale and for particular cloudy scenes (e.g., cumulus clouds).

The cloud fraction can be extended to an effective cloud fraction, $CF(\theta)$, dependent upon viewing angle, but retaining the same interpretation as the fractional area covered in clouds. The area of the earth with clear line of sight will shrink generally as θ increases [6]. A perfectly flat object will cast the same size shadow on a flat earth from dawn until dusk; the vertical dimension of the cloud will increase its shadow as θ increases. Figure 3-2 depicts the shrinking of the area with clear line of sight for a particular broken cloudy field.
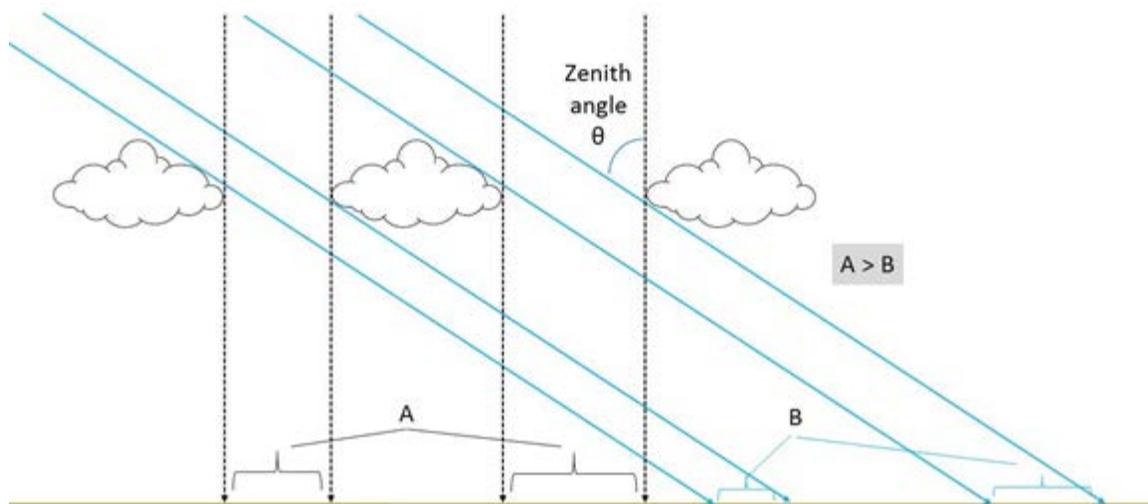
Figure 3-2. Schematic of the Dependency of PCFLOS on Viewing Angle
Because of clouds' vertical thickness, the visibility through a broken cloud deck will generally decrease with viewing angle off zenith (A>B).

Unfortunately, realistically defining the spatial dimensions of the 3D space of clouds is especially challenging and not well supported by direct observation. Similarly, defining

the spatial extent of a cloud is generally ambiguous. Past work estimating angular dependence of PCFLOS typically does not make individual measurements of CFLOS (say, from an aircraft), but rather uses an algorithm based upon photographs [1], or a ground instrument [5, 8], averaging visibility in a scene in a similar way to that mentioned above. A common technique to bound the problem is to restrict study to a single layer of cumulus clouds. Two studies published in 2004 and 2008 found good agreement between ground-observed PCFLOS at a location in the tropical, western Pacific and the Southern Great Plains to PCFLOS modeled using random, Poisson distributed hemispheres to represent clouds [6, 8]. Under these conditions, the PCFLOS through a cumulus field is modeled as,

$$PCFLOS_{cumulus} = (1 - CF)^{f(\theta)} \tag{3-4}$$

where

$$f(\theta) = \frac{1}{2}\left(1 + \sqrt{1 + \tan^2\theta}\right) \tag{3-5}$$

and CF is the cloud fraction at zenith. Naively using this equation to estimate PCFLOS given a particular cloud fraction is not recommended, since typical cloud formations vary from location to location, and the classification of clouds into cumulus and stratus types is not rigorous [10].

In summary, the PCFLOS metric is a practical metric that provides useful information on the expected operating conditions a sensor may experience. The metric is typically constructed using past observations. PCFLOS depends sensitively on many factors such as target location and season. Since PCLFOS is a statistical measure, care must be taken to assure that the sampling dataset used to generate the metric is consistent with the way in which it will be used.

References

1. Lund, I. A. and M. D. Shanklin, "Photogrammetrically determined cloud-free lines-of-sight through the atmosphere," *Journal of Applied Meteorology*, 11(5):773– 782, 1972.

2. Institute for Defense Analyses, *Cloud-free line-of-sight (CFLOS) availability*, IDA Paper P-2655, 1992, UNCLASSIFIED.

3. Institute for Defense Analyses, *Estimates of probability of a cloud-free line-of-sight for Raptor Talon*, IDA Paper D-1442, 1994, UNCLASSIFIED.

4. Venkat, R. A. and D. W. Young, "Cloud-free line-of-sight estimation for free space optical communications," *Proc. of SPIE*, volume 8732, pages 873205–1, 2013.

5. Shields, J. E., A. R. Burden, R. W. Johnson, M. E. Karr, and J. G. Baker, "Measurement and evaluation of cloud free line of sight with digital whole sky imagers," *The Battlespace Atmospheric and Cloud Impacts on Military Operations (BACIMO) Conference*, 2005.

6. Ma, Yingtao, "Longwave radiative transfer through 3d cloud fields: testing the probability of clear line of sight models with the arm cloud observations" (PhD diss., University of Maryland, College Park, 2004).

7. Killen, R. M. and R. G. Ellingson, "The effect of shape and spatial distribution of cumulus clouds on longwave irradiance," *Journal of the atmospheric sciences*, 51(14):2123–2136, 1994.

8. Taylor, P. C. and R. G. Ellingson, "A study of the probability of clear line of sight through single-layer cumulus cloud fields in the tropical western Pacific," *Journal of the Atmospheric Sciences*, 65(11):3497–3512, 2008.

9. Stubenrauch, C.J., W.B. Rossow, S. Kinne, S. Ackerman, G. Cesana, H. Chepfer, L. Di Girolamo, B. Getzewich, A. Guignard, A. Heidinger, et al., "Assessment of global cloud datasets from satellites: Project and database initiated by the GEWEX radiation panel," *Bulletin of the American Meteorological Society*, 94(7):1031–1049, 2013.

10. Wang, Pao, *Physics and dynamics of clouds and precipitation*, Cambridge: Cambridge University Press, 2013.

4.   Select Satellite-Based Datasets

Satellites provide an unprecedented platform through which to measure the radiative properties of the atmosphere on a global scale. The scientific datasets used in this study are based primarily upon radiation measurements from equipment housed in the "A-train" constellation of satellites. The constellation consists of the satellites Aura, CloudSat, CALIPSO, Aqua, GCOM-W1, and OCO-2, each housing distinctive scientific equipment (see Stephens et al. for a scientific summary of the A-train [1]). The constellation performs an approximately 99-minute sun-synchronous orbit, returning to the same orbit about every 16 days (233 orbits in 16 days). The instruments housed in the satellites make virtually simultaneous measurements of the earth's surface, allowing the unique capabilities of the instruments to be combined in scientific studies.

Figure 4-1 depicts two sample orbits of the CloudSat satellite, flying in the A-train. Notice that upon completion of a single orbit, the satellite is displaced hundreds of miles from its original location. The constellation passes the equator northbound at approximately 1:30 p.m. local time and southbound at approximately 1:30 a.m. local time. Thus, the A-train constellation provides measurements at about two times of day for a particular location.
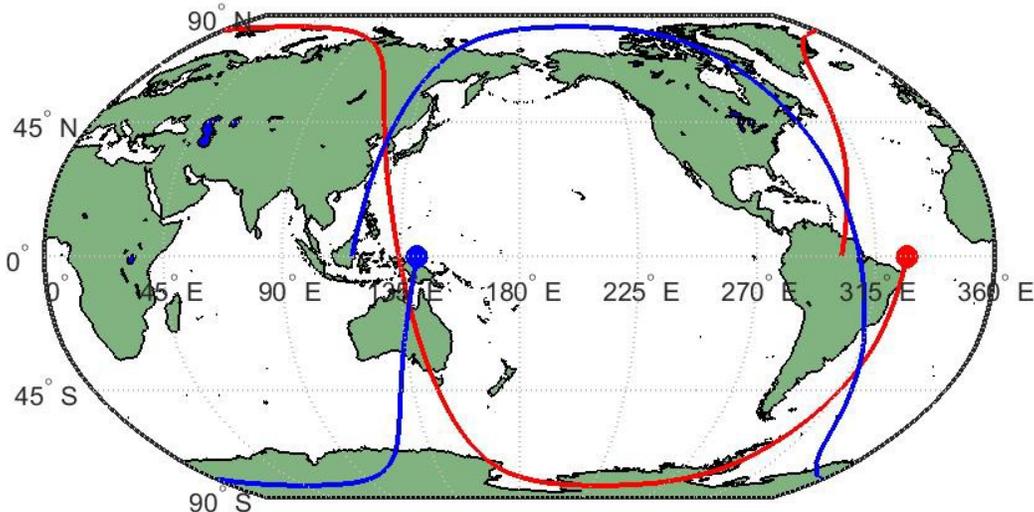
**Figure 4-1. Sample Orbit Paths of the CloudSat Satellite
in the A-Train Constellation of Satellites**

The dots denote the start of the orbits. The red orbit passes North Korea in the afternoon, and the blue orbit in the early morning.

A. CloudSat and CALIOP

Colorado State's CloudSat project provides years of global satellite-based cloud observations. The CloudSat satellite houses the Cloud Profiling Radar (CPR), an active radar system designed to penetrate through moisture and profile multiple cloud layers. The CPR operates on the long-wave wavelength of 3,400 µm (94 GHz) with a pulse width of 3.3 µs. The CPR is nadir-pointing, leaving an effective footprint of about 1 km along the orbit of the satellite and about 1 km perpendicular to the orbit. The vertical profile of the atmosphere is sampled with a resolution of about 250 meters. CloudSat nominally has a vertical resolution of 485 meters, but over-sampling effectively doubles this resolution [2]. The signal suffers small, but measurable, attenuation from cloud droplets, ice particles, and even raindrops. All scientific products offered from the CloudSat project are based upon the measured radar backscatter as a function of altitude.

The satellite CALIPSO operates a similar device called the CALIOP (cloud-aerosol lidar with orthogonal polarization). The CALIOP pulses on the shorter wavelengths of 0.532 and 1.06 µm in the visible and near-infrared bands. As discussed in Chapter 2, at these frequencies cloud droplets will strongly scatter incoming radiation. The signal will attenuate passing through significant cloud cover. The CALIOP is also nadir-pointing and leaves a smaller effective footprint than CPR but is more often sampled [1, 3]. Similarly to the CPR, the CALIOP system measures the lidar backscatter as a function of altitude.

The CPR and CALIOP systems provide symbiotic measurements of clouds and water vertical layers in the earth's atmosphere. The CALIOP, operating on the visible and near-infrared frequencies, is more sensitive to cloud layers than the penetrating CPR, which can measure vertically deep clouds. CloudSat's CPR cannot accurately detect hydrometeors below 1 km. CloudSat researchers Gerald Mace and Qiuqing Zhang identify the following technical limitation of the combined instruments: clouds below optically thick clouds might be missed when they are weakly reflective or under 1 km in height [3].

Since the CPR and CALIOP systems only sample at nadir, persistent gaps on the surface of the earth remain unmeasured by the combined systems. Figure 4-2 depicts the ground trace of an ensemble of CloudSat orbits. The sun-synchronous orbit of the A-train is designed to repeat its "ground track" every 16 days; of the 233 typical ground tracks for each full 16-day orbit, 16 that pass through North Korea are shown. Over 1,000 unique orbits are depicted in the figure, but they can clearly be organized into 16 typical orbits, 8 red and 8 blue.

The CloudSat project provides post-processed products of clouds' optical and physical properties. These products include the raw, backscattered radar power as a function of elevation (1B-CPR), a geometric grid of cloud locations (2B-GEOPROF, 2B-GEOPROF-LIDAR), an identification of cloud types (2B-CLDCLASS-LIDAR), cloud optical depth (2B-TAU), and cloud liquid and ice water content (2B-CWC-RVOD) among other scientific products. The "-LIDAR" suffix indicates that CALIOP data are combined with the CPR to produce the product. All products are free to download from Colorado

State's website (http://www.cloudsat.cira.colostate.edu/data-products), with scientific publications and technical details for each product provided.
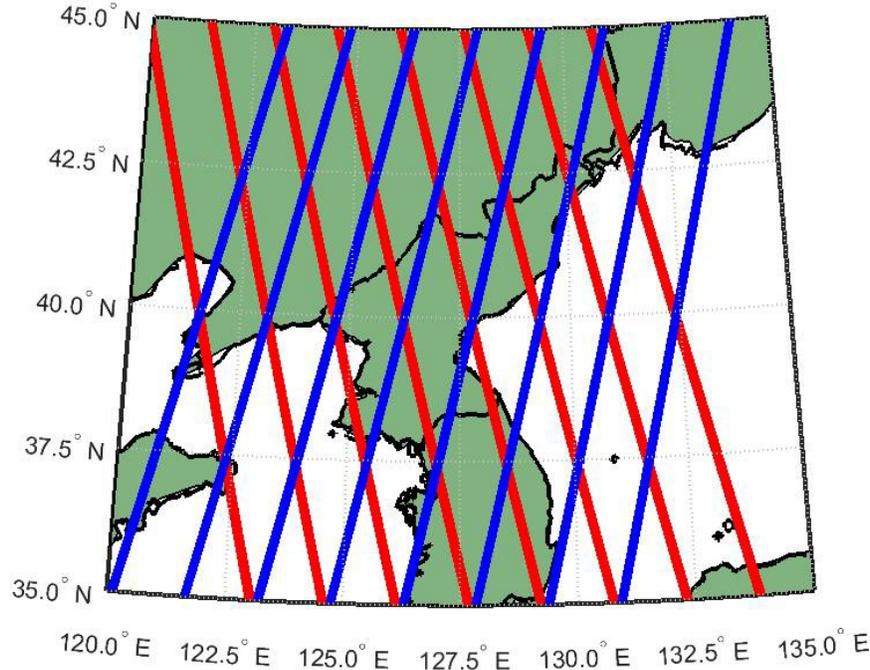
Figure 4-2. Ground Tracks of 1396 CloudSat Orbits that Pass Near North Korea
Orbits heading northbound and passing North Korea in the afternoon are marked red, and those heading southbound in the early morning are marked blue. The orbits are grouped into 16 nominally identical paths, easily identified in the graph as thick lines.

We used the dataset recording a geometric grid of clouds locations, 2B-GEOPROF-LIDAR, for the first case study presented in this report (Section 5.A). Figure 4-3 depicts a sample granule of data taken from a single orbit of the A-train. Each location in the grid is marked with a "cloud fraction," a value between 0 and 1 that denotes the fractional presence of a hydrometeor (rain or cloud) using information from both CloudSat and CALIOP. CloudSat's algorithm for determining the presence of a cloud is based upon comparing the radar backscattering power (using the radar equation) to the noise background.[1]

The combined radar-lidar products maintained by CloudSat provide a view of the vertical profile of clouds in the earth's atmosphere. The main weaknesses to this dataset are the persistent gaps depicted in Figure 4-2, the long revisit time, and the relatively small geographical footprint cross-path (approximately 1 km). These data provide a two-dimensional view: the dimension along the path of the satellite and the vertical dimension. The unique accuracy and penetrating power of the two pieces of equipment thus provides

---

[1]   For the primary academic publications on the product, see Marchand et al. [4] and Mace and Zhang 2014 [3], and for technical details on the algorithm, see CloudSat's technical manual for the 2B-GEOPROF and 2B-GEOPROF-LIDAR products on their website.

"the first measure of global cloud vertical structure that is not limited by the presence of optically thick layers near the tops of cloudy columns" [3].
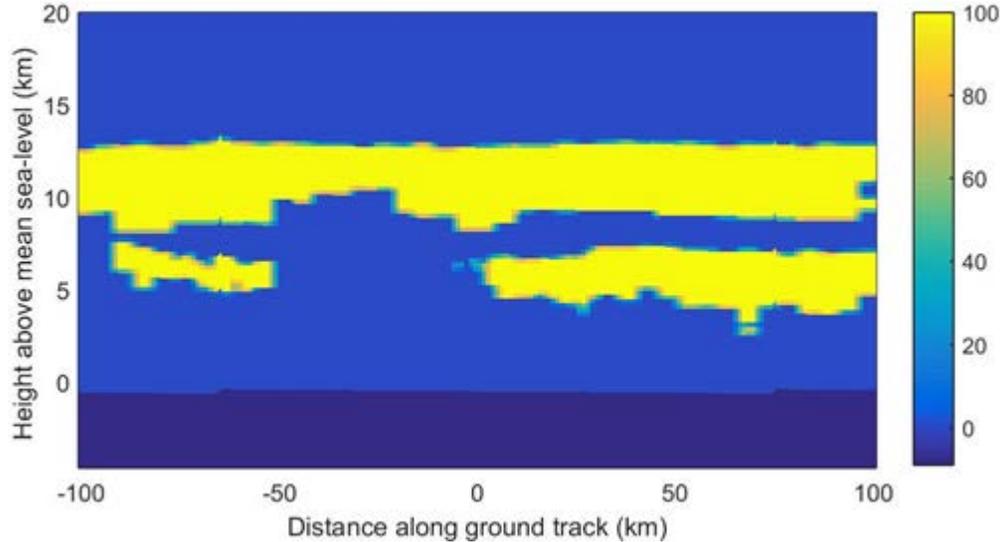
Figure 4-3. Sample Granule from 2B-GEOPROF-LIDAR Product: Clouds Detected by the Combined CloudSat and CALIPSO System, along an Orbit near Kujang, North Korea

X-axis denotes distance on plane of the earth along the path of the satellite, with zero being the minimum distance on the track from Kujang (39.9 ºN, 126.25 ºE). Y-axis denotes elevation above mean sea level. Yellow shading denotes clouds; blue shading, open sky; and any color in-between, cloud volume fraction.

B. MODIS

NASA's MODIS is housed on the satellites of Aqua and Terra. The Aqua satellite orbits in the "A-train" constellation; the Terra satellite performs a very similar sun-synchronous orbit, crossing the equator northbound at about 10:30 p.m. and southbound at 10:30 a.m. local time. MODIS acquires data using passive sensors (detecting natural radiation) operating on 36 spectral bands observing up to ± 55º from nadir, with a spatial resolution of 250 meters, 500 meters, and 1 km along and across the satellite path at nadir. Because of the observational zenith angle, this resolution is about a factor of five coarser at angles farthest from nadir. The two instruments each completely measure the earth's surface every 1 to 2 days.

MODIS's CloudMask product provides results from a series of spectral tests designed to detect clouds. The product contains results from 14 spectral bands, four of which are directly used to detect the presence of a cloud. The remaining spectral tests are leveraged by the cloud detection algorithm to determine an appropriate confidence level given the particular situation (the presence of sun-glint for example). Through this algorithm, the MODIS science team provides a best estimate on whether or not a cloud was detected at a particular location and their confidence in that detection. (For the case studies presented in this report, if the MODIS science team was 66 percent sure of cloud-free sky, we assumed no cloud was present. The most common confidences in detection are above 95 percent. Robert Wood et al. found their analysis on clouds' horizontal distributions using

this dataset were consistent regardless of whether or not they interpreted uncertain pixels as being cloudy or clear [5].)

Figure 4-4 displays a granule of CloudMask data from 17 January 2014, depicting the clouds north of Japan. Because of the high speed of the orbiting satellite, the clouds pictured in Figure 4-4 are imaged minutes apart.
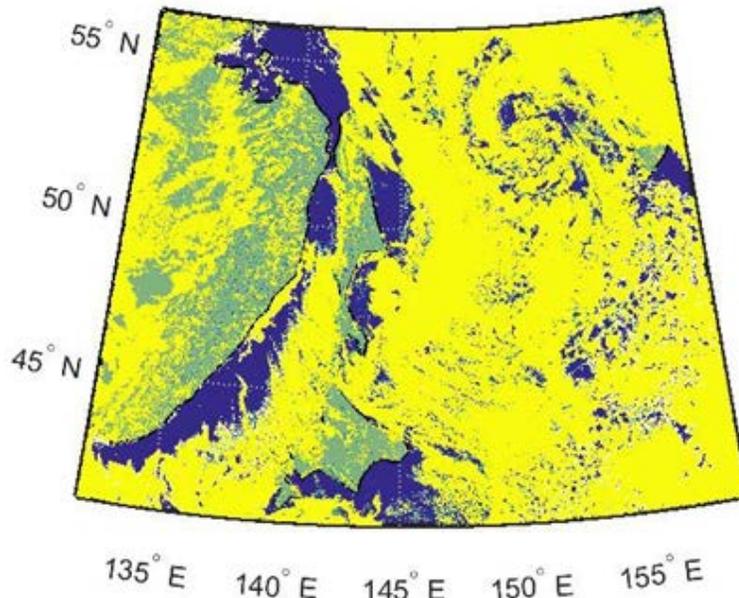
Figure 4-4. Clouds Detected by MODIS North of Japan on 17 January 2014

Yellow denotes clouds; blue, open water; and green, open ground. Notice the fine spatial structure captured by MODIS, as well as the prevalence of large, connected cloudy regions.

MODIS's dataset provides standardized, high-quality, and high-resolution data of historical weather patterns anywhere on the globe. Because of its importance in informing climate modeling, the quality and consistency of the MODIS dataset is a continuing focus of MODIS's science team. The CloudMask algorithm was validated in 1998 in a case study [6], and in a recent study, the global MODIS cloud dataset compared favorably with other independently gathered satellite cloud databases [7]. As mentioned above, for each CloudMask datum, the MODIS team documents its confidence in quality of the data, cross-validating spectral tests and considering factors such as the prevalence of sun glint or snow. This transparency allows the user to control and document the desired level of confidence in studies based upon the MODIS dataset.

The MODIS global cloud database provides much greater spatial coverage than the CloudSat database. The revisit time for a location is much shorter as a result. However, MODIS's database is still a two-dimensional view: the dimension along the path of the satellite and the dimension across the path. Although MODIS estimates the cloud top height using CO_2 slicing [8], we have not incorporated this information into our analysis since it provides a rough and incomplete picture of cloud's vertical structure. The MODIS CloudMask dataset's greatest strengths are the planar spatial correlation of clouds and the sheer quantity of data for any location in the world.

References

1. Stephens, G. L., D. G. Vane, R. J. Boain, G. G. Mace, K. Sassen, Z. Wang, A. J. Illingworth, E. J. O'Connor, W. B. Rossow, S. L. Durden, et al, "The CloudSat mission and the A-Train: A new dimension of space-based observations of clouds and precipitation," *Bulletin of the American Meteorological Society*, 83(12):1771–1790, 2002.

2. Tanelli, S., S. L. Durden, E. Im, K. S. Pak, D. G. Reinke, P. Partain, J. M. Haynes, and R. T. Marchand, "CloudSat's cloud profiling radar after two years in orbit: Performance, calibration, and processing," *IEEE Transactions on Geoscience and Remote Sensing*, 46(11):3560–3573, 2008.

3. Mace, G. G. and Q. Zhang, "The CloudSat radar-lidar geometrical profile product (RL-GeoProf): Updates, improvements, and selected results" *Journal of Geophysical Research: Atmospheres*, 119(15):9441–9462, 2014.

4. Marchand, R., G. G. Mace, T. Ackerman, and G. Stephens, "Hydrometeor detection using CloudSat-An Earth-orbiting 94-GHz cloud radar," *Journal of Atmospheric and Oceanic Technology*, 25(4):519–533, 2008.

5. Wood, R. and P. R. Field, "The distribution of cloud horizontal sizes" *Journal of Climate*, 24(18):4800–4816, 2011.

6. Ackerman, S. A., et al., "Retrieval of effective microphysical properties of clouds: A wave cloud case study," *Geophysical research letters* 25.8: 1121-1124, 1998.

7. Stubenrauch, C.J., W.B. Rossow, S. Kinne, S. Ackerman, G. Cesana, H. Chepfer, L. Di Girolamo, B. Getzewich, A. Guignard, A. Heidinger, et al., "Assessment of global cloud datasets from satellites: Project and database initiated by the GEWEX radiation panel," *Bulletin of the American Meteorological Society*, 94(7):1031–1049, 2013.

8. Ackerman S., K. Strabala, P. Menzel, R. Frey, C. Moeller, and L. Gumley, "Discriminating clear-sky from cloud with MODIS algorithm theoretical basis document (MOD35)," *MODIS Cloud Mask Team, Cooperative Institute for Meteorological Satellite Studies, University of Wisconsin*. Citeseer, 2010.

5.   Case Studies

A. Estimating PCFLOS Using CloudSat and CALIPSO

In the summer of 2015, we explored how the viewing angle affects the probability of cloud-free line of sight. This work was conducted for the Global Hawk Program Office.[1] As mentioned in Chapter 3, the decrease in visibility through a scattered cloud field is a well-explored effect, with a history of experimental and modeling work in the defense community. A past study of probability of cloud-free line of sight over the globe by CloudSat researcher Don Reinke drew our attention to the CloudSat database and the unique vertical profiling it provides [2]. We used this global study as motivation for our own detailed analysis of PCFLOS at four separate geographical locations.

Don Reinke's study estimates PCFLOS using a line of sight calculation on a series of geometric grids of clouds (the 2-B GEOPROF dataset). The details of his calculation and the construction of a probability from a series of observations can be found in a proceedings paper [2]. While it is well established in the literature that cloud-free line of sight decreases with viewing angle [3-7], PCFLOS as a function of viewing angle reported in this dataset is typically non-monotonic. (We suspect that sampling issues led to this result, potentially resulting from averaging along lines of sight both in the forward and backward direction of the path of the satellite.) One major motivation for performing our own analysis of the CloudSat database was to rectify this inconsistency with the literature.

Using sets of geometrically gridded clouds, or snapshots of weather, at four separate geographical locations, we designed a line-of-sight algorithm to identify the frequency of cloud blockages. Appendix A details the algorithm and its modeling assumptions. The result of the algorithm is an estimate for PCFLOS, calculated in a similar manner to Eq. 3-3 and defined as a function of season, day or night, altitude of observer, and viewing angle (angle off zenith). Table 5-1 summarizes this parameter space.

Table 5-1. Parameter Space of the PCFLOS Metric Calculated for this Case Study

Param	Season	Day, Night	Altitude of Obs.	Viewing Angle
Domain	Winter (DJF), Spring (MAM), Summer (JJA), Fall (SON)	1:30 am, 1:30 pm	1 km to 25 km, 1 km steps	0° to 80°, 5 steps

PCFLOS was calculated using a line-of-sight algorithm for four locations of interest in the world. The data used in this study came from CloudSat's 2B-GEOPROF-Lidar product, with data spanning 6 calendar years (2006-2011).

---

[1]   See previous IDA study [1].

Using approximately 5 years of data from Colorado State's CloudSat project, stretching from 2006 to 2011, we can estimate PCFLOS anywhere in the globe. We selected four particular locations, areas of interest to the U.S. Department of Defense, to demonstrate the information we can extract from this procedure: Kujang, North Korea; Donetsk, Ukraine; Qom, Iran; and Maradah, Libya. While each country was selected because of geopolitics, the particular locations in each country are near a crossing point of typical northbound and southbound orbits (see Figure 4-2 and Radha Venkat's 2013 study [8]). By selecting a target near this crossing point, we increase the quantity of data available for the study and decrease the distance between the satellite tracks of the orbits. Only those orbits that passed within 25 km of the targets were used in the study.

1.   Study of Clouds Over Kujang, North Korea

Figure 5-1 depicts the seasonal variation in PCFLOS at nadir of an observer over a range of altitudes at a specific location in North Korea.
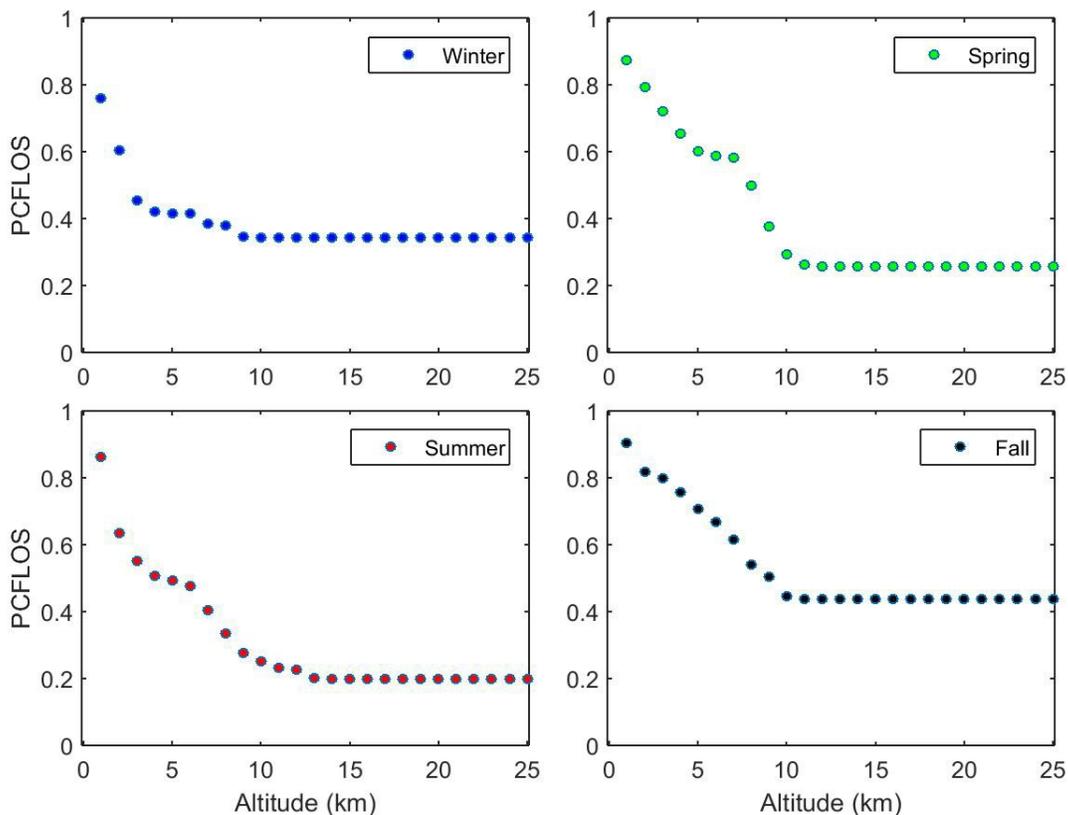
Figure 5-1. PCFLOS vs Altitude of Observer at Nadir: Seasonal Variation Near Kujang, North Korea (39.9 °N, 126.25 °E)

Observations taken from CloudSat's GEOPROF-Lidar database [10], using 84 individual observations over 3 years within 20 km of target. Fall tends to be the clearest season. Low-lying clouds are very common in winter, reflected in the low PCFLOS values near 3 km. Notice that above 13 km PCFLOS remains constant, reflecting that clouds are not observed at these altitudes.

With an observer directly above the target at nadir, PCFLOS will by definition decrease as a function of altitude; a cloud at a certain altitude will block line of sight for all

observers above it. The rate of change of PCFLOS with altitude is related to the presence of typical cloud layers at that location. For example, the upper left panel of Figure 5-1 depicts the dependence of PCFLOS on altitude for the 3 winter months of December, January, and February. The curve represents an unweighted average of cloud-free line of sight determinations on approximately 20 separate cloudy scenes. In the winter, PCFLOS dramatically decreases around 3 km in altitude, reflecting that low-altitude clouds are common in the winter. The lower right panel of the figure, corresponding to fall, displays a PCFLOS curve with a more consistent slope, indicating that in the fall, clouds are approximately uniformly common from altitudes of 1 km to 10 km.

Figure 5-2 depicts the angular dependency of PCFLOS near Kujang, North Korea. Our results indicate that altitude from 1 km to 12 km is a far more important parameter than angle of observation. The angle of observation has negligible effect between 0° and 45°, and at most appears to have a maximum effect of decreasing PCFLOS by 10 percent at lower altitudes and high angles.
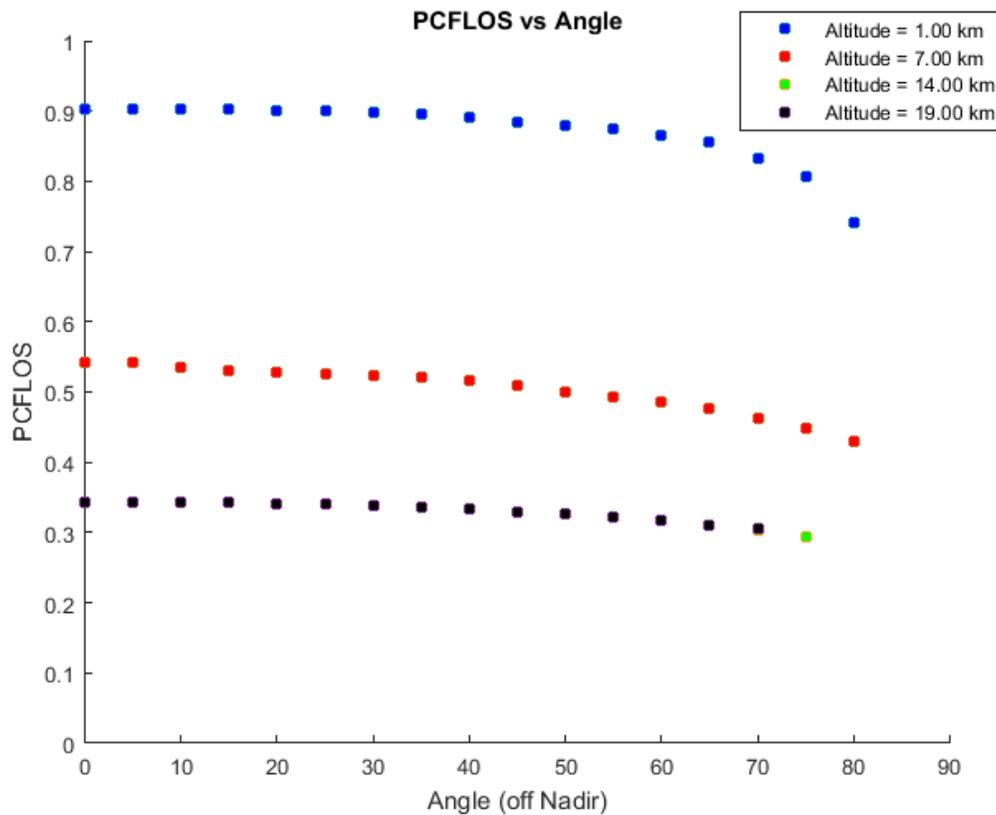
Figure 5-2. PCFLOS vs. Angle of Observation Near Kujang, North Korea (39.9 °N, 126.25 °E)

Observations taken from CloudSat's GEOPROF-Lidar database [10], using 84 individual observations over 3 years within 25 km of target. The two curves for PCFLOS vs. angle for altitudes of 14 km and 19 km lie on top of each other, reflecting that no clouds were detected between those altitudes. Observers were placed along a 50-km stretch of satellite track close to the target.

The other three locations studied demonstrated similar dependence of PCFLOS on viewing angle. Clearly altitude is a more important parameter for visibility than angle.

Figure 5-3 depicts the angular dependency of PCFLOS near Kujang, North Korea; Donetsk, Ukraine; Maradah, Libya; and Qom, Iran. The weak dependence of PCFLOS on viewing angle was surprising to us at first (the other three locations studied demonstrated similar dependence). Previous studies of actual cloudy fields have found stronger dependence on viewing angle either for particular cloudy fields or as functions of cloud fraction [4-8]. We believe the reason for us finding such dependency is twofold: the resolution of the CPR does not resolve gaps near or below 1 km in length, and we did not restrict our study to partially cloudy weather.
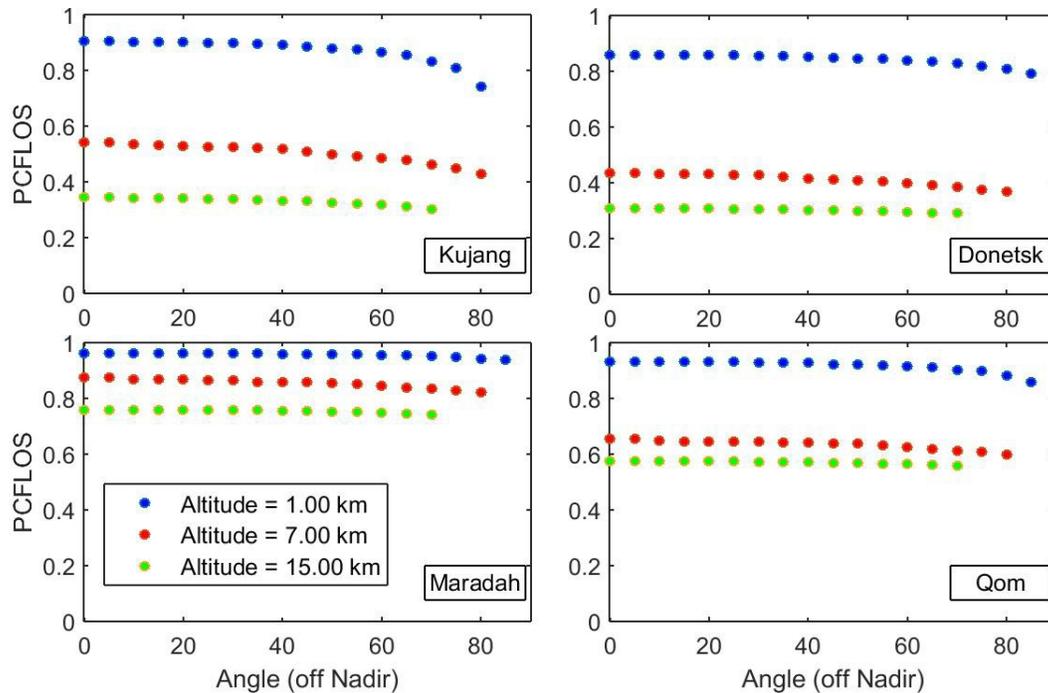
Figure 5-3. PCFLOS vs. Angle of Observation for Altitudes of 1 km, 7km, and 15 km for four Separate Locations: Kujang, North Korea (39.9 °N, 126.25 °E); Donetsk, Ukraine (48.5 °N, 38 °E); Maradah, Libya (29.2 °N, 19.5 °E); and Qom, Iran (34.6 °N, 50.5 °E)

Observations taken from CloudSat's GEOPROF-Lidar database [9], using observations over 5 years within 25 km of each target. Observers were placed along a 50-km stretch of satellite track close to the target.

Addressing the first point, the horizontal resolution of CloudSat's CPR is about 1.1 km. Thus gaps in the clouds around or below this length will not be resolved. The shutter effect of clouds discussed in Section 3.B will only yield variation in PCFLOS with angle if the gaps are well resolved. In 2013 Nico Trebbin performed a statistical analysis of gaps in clouds using measurements from the active lidar sensor onboard the satellite Calipso (see Section 4.A) with a horizontal resolution of 333 meters [10]. Based upon a full year of data with 14 million cloud gaps, Trebbin calculated a mean cloud gap of 7.41 km and a median of about 1 km. Thus, we expect CloudSat resolves around half the gaps between clouds that are large enough to be operationally relevant.

Concerning the second point, since we did not restrict our study to cumulus-type clouds, the preponderance of large, connected clouds will lessen angular effects.

Restricting our averaging to instances of weather with partly cloudy coverage would most likely increase the dependency of PCFLOS on angle.

Figures 5-1 through 5-3 depict the chance of a cloud blockage to a line of sight between an observer and the target. Multiple cloud layers could obstruct the view. Using CloudSat's cloud-detection and identification algorithm contained in product 2B-CLDCLASS-Lidar,[2] we can characterize these cloud obstructions. CloudSat sorts clouds into eight types: cumulus (Cu), stratocumulus (Sc), stratus (St), altocumulus (Ac), altostratus (As), nimbostratus (Ns), cirrus/cirrostratus (high cloud), and deep convective clouds. Each of these cloud types are, in part, defined by CloudSat to have a characteristic length scale; cumulus clouds have horizontal dimensions around 1 km and nimbostratus clouds range from 50 to 1,000 km in length. Figure 5-4 depicts the probability of occurrence for each observed cloud types near Kujang, North Korea.
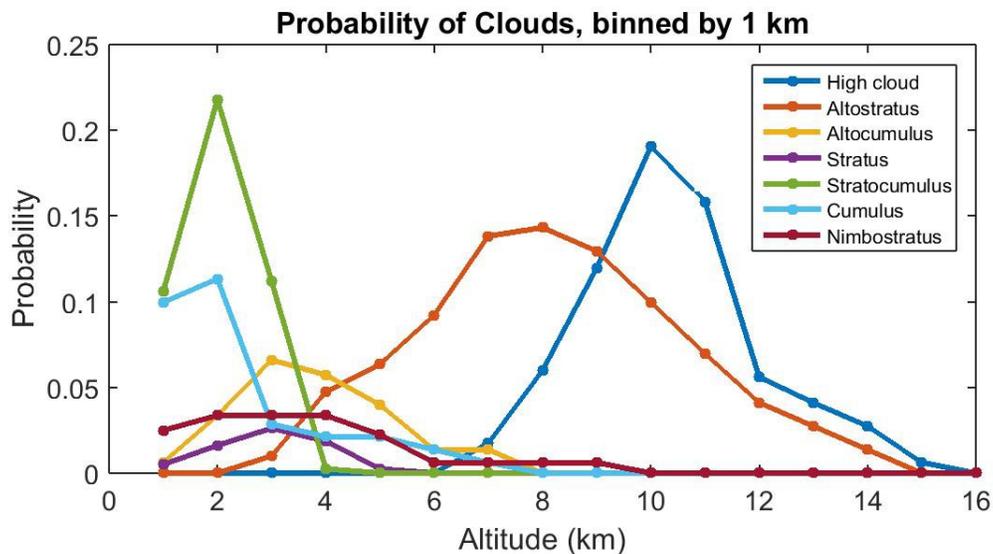
Figure 5-4. Probability of Cloud Occurrence, Sorted By Type Near Kujang, North Korea (39.9 ⁰N, 126.25 ⁰E)

Observations taken from CloudSat's CLDCLASS-Lidar database [11], using 73 individual observations over 3 years within 25 km of target. Clouds are correlated by altitude. The size of clouds obstructing Kujang varies from small cumulus clouds to giant nimbostratus clouds (deep convective clouds not shown).

2. Weaknesses and Strengths of the Study

The limitations of the PCFLOS metric calculated in this study arise primarily as a result of limitations of the CloudSat database instead of our analysis of the database. As discussed in Section 4.A, CloudSat does not completely image the globe; the instances of weather that are associated with one of the four locations explored in this case study are located only within 25 km of each other. Thus we are capturing the characteristic weather of each location and assuming that local variability in PCFLOS is marginal. In addition, clouds are only resolved to 1 km, and smaller clouds and clouds below 1 km in height are

---

[2] See Sassen, Wang, and Liu 2008 [11].

liable to be missed. As discussed in the previous subsection, not resolving the gaps between clouds will limit some dependency of PCFLOS on viewing angle. Also, the observations from CloudSat are restricted to two times of day; daily variability in cloud cover cannot be captured.

The matrix of clouds used in the study represents a 2D picture of a 3D world; the angle of observation only represents the direction along the path of the satellite. We suspect that PCFLOS versus viewing angle will vary with respect to bearing. It is probable that certain areas of the world have clouds organized in characteristic directions, but we found little variation with respect to viewing angle in our four locations cases. In addition, Wood et al. found that the statistical properties of cloud sizes do not vary when measuring along-track as opposed to across-track [12]. Wood et al. were using MODIS's CloudMask (discussed in Section 4.B), and both satellites that house the MODIS equipment operate on similar orbit paths as CloudSat and CALIOP. As a counterpoint, in our study of clouds' spatial distributions in the Baltic, we found noticeable dependence of clouds' spatial distributions on bearing (see Section 5.C for details). Potentially, additional studies could combine information from both methods discussed in this CloudSat-based study and the study on the Baltic using MODIS's dataset, providing a more complete measurement of 3D cloud fields.

Despite these weaknesses, the probability of cloud-free line of sight derived in this case study allows us to represent typical cloud patterns that occur at any location in the world. The information we can extract accurately quantifies the vertical structure of clouds, allowing us to predict typical cloud decks' elevations and the expected change of visibility with altitude. In addition, we can group expected cloud blockages into frequencies of occurrence for specific cloud types separating monsoons from fair-weather cumulus clouds.

B.   Cloud Modeling in ISEE Using MODIS

To analyze the effect of environmental conditions on imagery collection, we developed a cloud modeling addition to our ISEE model [13]. ISEE simulates imagery collection at the mission level, modeling aspects of the exercise including, but not limited to, sensors, targets, atmospherics, geography, and scheduling. The goal of our cloud-model addition was to estimate the role clouds have on inhibiting information extraction from multiple targets with multiple sensors on the time scale of hours on length scales up to hundreds of kilometers.

The new cloud model is designed to take two-dimensional cloud grids from NASA's MODIS CloudMask dataset. These grids specify in a roughly 1 km × 1 km grid the location of clouds at a given instant on a particular day. This information is used in ISEE's line-of-sight calculation, with the presence of a cloud in that line of sight assumed to completely obscure information extraction. By using an ensemble of actual weather patterns and running ISEE multiple times with different grids of clouds, we estimate the degree to which clouds might hamper imagery collection.

1. Details of Cloud Model

Using historical weather patterns captured by NASA's MODIS, we performed an ensemble of simulations to determine the effect of cloud cover on our imagery collection model ISEE. Figure 4-4 depicts one such "snapshot" of clouds north of Japan. Each instance of weather extracted from the MODIS dataset provides realistic operating conditions. By running an ensemble of simulations, we can determine how the model is affected by particularly cloudy, clear, and typical weather over the entire country. Thus, we can determine not only the average effect of clouds, but also the best and worst case effects.

Each cloudy scene extracted from MODIS covers the entire country in question. The MODIS dataset is packaged into granules corresponding to an orbit of the satellite. Restricting the data to the country in question, we create a spatial grid that records for each grid point whether or not a cloud is present. The resolution of the dataset is approximately 1 km × 1 km directly underneath the satellite's path, and up to 5 km in width at the edges of the grid. At the initialization of the simulation, we associate each target with the nearest cloud grid point and record whether a cloud is present. If a cloud is present, we consider that target blocked, and no imagery collection can occur. As ISEE runs, we simulate the movement of clouds via wind using the static turbulence model: wind translates the clouds without changing their relationship to each other. Each time the wind translates the clouds, each target is reassociated with the nearest cloud grid point. Thus, the average in time is the same as the instantaneous spatial average.

Our strategy for cloud modeling prioritizes spatial fidelity. MODIS provides an accurate estimation of which targets are blocked at a particular time. Thus, we can estimate not only the chance of a target being blocked, but the chance that another target is blocked concurrently. This has obvious implications for simultaneous tracking of multiple targets in a geographical region. For instance, by considering dozens of instances of weather over the country of interest in February, we have an estimate for the likelihood of practically full cloud cover over the country and the information that can be extracted (if any) under those circumstances.

2. Justifications for Modeling Procedure

For this case study, we did not use a data-based estimate of PCFLOS to generate predictions. The imagery collection simulation in ISEE conducts multiple near-simultaneous observations of targets that could be very close or very far away. Thus, weather affecting each observation is correlated. For example, say the probability that a particular location is cloud covered is 50 percent and the probability that a location 2 km away is covered is also 50 percent. However, to simulate imagery collection, the existence of a cloud blockage must be determined. Given a cloud blockage at one location, there is a higher than 50-percent chance that the second location is blocked by clouds. This is due to the fact that clouds are spatially correlated. The MODIS dataset provides excellent spatial distributions of clouds on the earth's plane, capturing their spatial correlation

explicitly to an accuracy of about 1 km. The CloudMask product is nominally available for spatial resolutions of 250 meters, 1,000 meters, and 5,000 meters. We selected the 1,000-meter spatial resolution for this study because it is fine enough to resolve gaps between clouds but is still computationally manageable.

The nadir-pointing satellites of CALIPSO and CloudSat provide detailed measurements of cloud thickness, elevation, and profile. However, they image only a 1-km wide strip of the earth's surface during orbit. The resulting cloud datasets are well resolved in the vertical direction and in the direction of the orbiting satellite, but provide no information in the direction perpendicular to the satellite path. MODIS provides a two-dimensional portrait of the clouds in the plane of the earth's surface, although it contains little information on cloud's vertical profiles. We identified the plane of the earth's surface as the most important dimensions to capture clouds in ISEE.

Due to the high speed of the orbiting satellite (the Aqua satellite completes an orbit about every 99 minutes), clouds within hundreds of kilometers are detected by MODIS within minutes of each other. Since the geographical area we wish to simulate has dimensions of hundreds of kilometers, we treat the detected clouds as existing simultaneously. A location is within the satellite's field of regard ($\pm 55°$ from nadir) every couple of days, and thus the time resolution of the dataset is much poorer than the spatial resolution.

The modeling strategy of ISEE with the cloud model addition is not to represent the real world with the highest fidelity possible, but rather to model a scenario with fidelity high enough to allow for meaningful comparisons between equipment, procedures, and other variables. Our method of introducing time dynamics into our cloud field is far from ideal, but it allows us to capture the quantitative effects of cloud coverage and gaps in cloud coverage on a large scale. We opted to sacrifice time-resolution for spatial resolution and used the static-turbulence model [14], which was discussed at the beginning of Section 3.B. This holds that spatial correlation is equivalent to time-correlation; as time passes, clouds translate in space. The longer the simulation runs, the less accurate the cloud simulation becomes. We care most about capturing the breaks in clouds and estimating how often and how many targets will be covered by clouds at a given time.

C. Cloud Distributions in the Baltic Region Using MODIS

In the winter of 2016, the Office of Cost Assessment and Program Evaluation (CAPE) requested that IDA perform a study on intelligence, surveillance, and reconnaissance (ISR) systems when applied to the Baltic region of Europe. Of particular interest was the ability of these systems to monitor U.S. and allied ground forces in the region. Cloud cover plays a role in remote surveillance, as EO/IR sensors are incapable of seeing through clouds. To explore the role of cloud cover in this scenario, we identified the following topics of analysis for the study: the change of average cloud coverage with month and location and the likelihood of multiple locations being covered in clouds simultaneously. To address these questions, we decided to perform an analysis of cloud distributions using MODIS's

CloudMask dataset [15]. This work leveraged the experience gained in performing the previous two case studies.

1.   Processing of the Dataset

The four calendar years of 2012-2015 were selected to form the observational basis for the study. We extracted 937 cloudy scenes represented in MODIS's CloudMask product, corresponding to about 80 granules of data per month. With such an abundance of data, we could generate good statistics on inter- and intra-monthly variability of cloud cover.

The "Baltic region" used in this study is pictured in Figure 5-5, originally defined as extending from 20° to 30° in longitude and 53° to 60° in latitude.
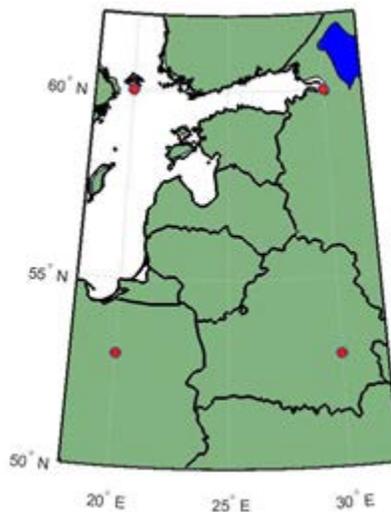
Figure 5-5. Region of the Earth Considered in This Study

Red dots denote the four corners of a rectangle in longitude and latitude, with the interior of this rectangle denoting the domain of the analysis.

Although the region is rectangular in terms of degrees, since the surface of the earth is a sphere, the region does not map perfectly to an evenly spaced rectangular grid. Notably, the east-west distance along the surface of the earth from one end to the other at the most southerly point is 670 km and at the most northerly point 560 km. The north-south distance along lines of longitude is 778 km. The autocorrelation analysis of clouds placed on a grid, which is presented later in this section, requires a regularly spaced grid. In such a grid, the distance between two pairs of indices depends only upon the relative difference of the indices. To convert our rectangular in degree grid to a rectangular in distance grid, we designed a simple coordinate projection. The new rectangular distance grid is 560 km × 778 km, obtained by removing two small triangles in the lower left and lower right of the region in Figure 5-5, and by changing the region from an apparent pentagon to an apparent rectangle. The new grid has an equal spacing of 750 meters in each direction. The binary matrix of clouds from MODIS's CloudMask product originally

defined in terms of degrees was interpolated onto the new grid using a nearest neighbor algorithm.

2.   Average Cloud Cover by Month and Location

We define the cloud fraction over the Baltic region as the fraction of the region covered in clouds. The median of this metric captures the typical amount that the Baltic is covered in clouds at any given time, as measured using this sample dataset. The left panel of Figure 5-6 depicts the distribution of this metric over the full dataset; the right panel depicts the monthly statistics of this metric, plotting the mean and 80-percent confidence bounds.
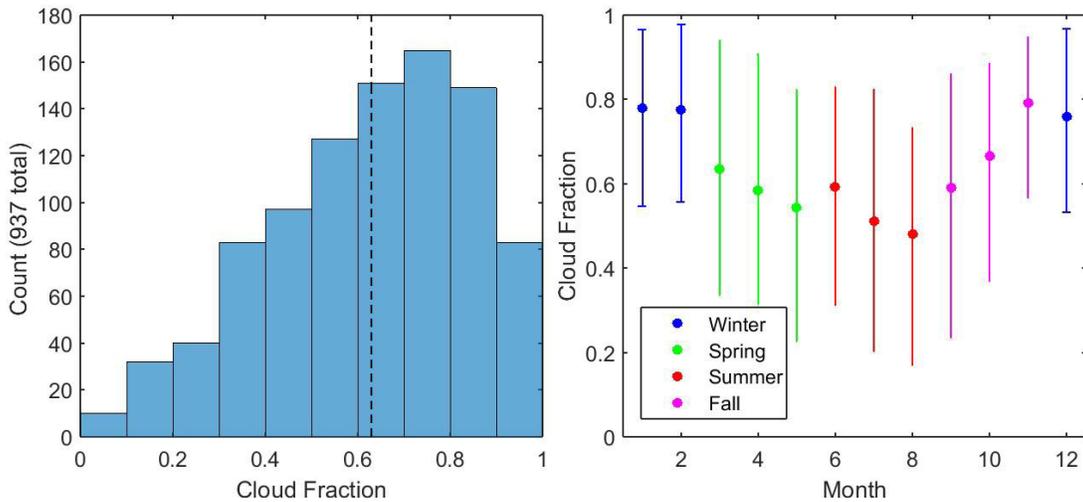
Figure 5-6. Amount the Baltic Is Covered in Clouds at any Given Time

(Left) Distribution of cloud fraction of the Baltic region for the full dataset considered in this study. The dashed black line denotes the mean cloud fraction of 0.63. (Right) Cloud fraction of the Baltic region versus month of the year. The mean cloud fraction is marked as a blue dot, with the upper and lower bounds indicating the middle 80 percent of the distribution. The statistics for each month were calculated using about 80 samples.

Figure 5-6 captures the variability of the cloud fraction in the Baltics. The region is more often covered in clouds than not, since the mean (and distribution generally) lies above a cloud fraction of 50 percent. During the winter months, clouds are especially common, with more than 95 percent of the region being covered in clouds more than 10 percent of the time. The variability in the cloud cover is quite striking, especially during the summer and spring months. This communicates a fact that we already intuitively know: at any given time of the year, there is a reasonable chance that it will be cloudy and there is a reasonable chance that it will be clear. This variability holds true even on scales as large as the Baltic region [12, 14].

Instead of averaging the occurrence of clouds over a geometric region and observing how this changes in time, we can average over time and observe how this changes with location. This time-averaged cloud frequency is depicted in Figure 5-7.
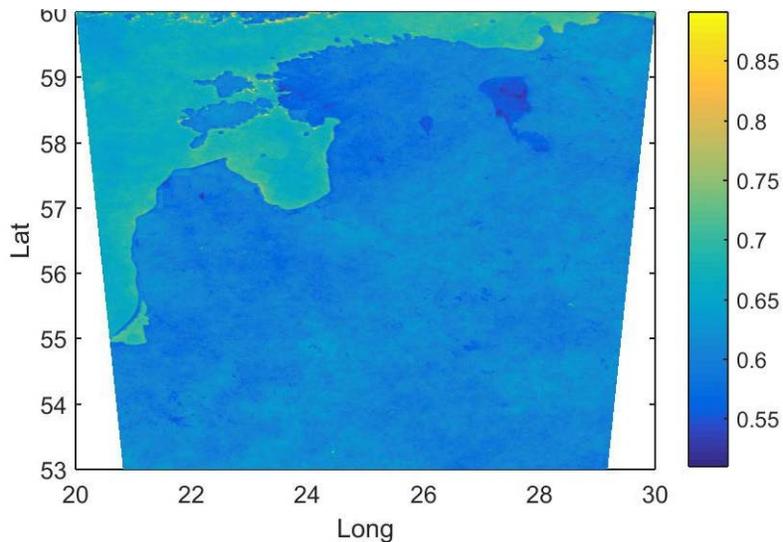
Figure 5-7. Time-Averaged Cloud Fraction of the Baltic Region

The higher frequency of clouds over the Baltic Sea makes the coast clearly visible. The inland Lake Peipus appears as a dark blob in the upper right of the figure, and it is unknown to us if clouds are in fact less common or more difficult to detect over the lake. The interior of the Baltic region varies in time-averaged cloud fraction from around 65 percent to 58 percent.

As visible in Figure 5-7, the variability in time-averaged cloud fraction is rather moderate over the land mass of the Baltic region. This suggests that year-round each land region has a similar number of cloudy days. Interestingly, the CloudMask product is sensitive enough to detect the exhaust from a building materials supplier factory in the Vaukavsky District of Belarus (53.27 °N, 24.44 °E). The smoke (aerosols) leaving the factory apparently is detected as clouds, leading to a local time-averaged cloud fraction of near 0.8, about 0.2 greater than the surrounding area.

3.   Spatial Correlation of Clouds

To quantify the tendency of clouds to cover vast swathes of land concurrently, we used the autocovariance metric. The autocovariance of a function measures its self-similarity with respect to change in independent variables. In our case, the function is the binary cloud matrix and the independent variables are the cardinal directions of east and north. We can use the autocovariance to determine the average change in cloud coverage with respect to distance in any planar direction. (See Appendix B for details of our analysis.)

Table 5-2 displays P_{same}, the chance of observing the same weather (cloudy or clear) a displaced distance from one's location, averaged over the years of 2012-2015. In the table, the second column lists the distance corresponding to each chance, averaged over all directions. The minimum and maximum distances are given in the third and fourth columns with absolute bearing listed in degrees. Clouds tend to be the most self-similar in the northeastern/southwestern direction, as evident in the bearings listed in the table. Figure 5-8 presents the same data in graphical form. The x-axis represents shifts along the cardinal directions of east (positive shift) and west (negative shift). The y-axis represents

5-11

shifts along the cardinal direction of north. P_{same} is symmetric with respect to the origin: comparing locations northwest is equivalent to comparing locations southeast. At zero distance, the weather is completely self-similar, and $P_{same} = 1$. As distance increases, the weather (cloud or clear) will be more and more likely to be different. Since clouds tend to exist in clusters, P_{same} decreases rather slowly as the distance increases. Even at distances of 200 km away, the likelihood of having the same "weather" is still around 70 percent.

Table 5-2. Chance of Observing the Same Weather (Cloudy or Clear) a Displaced Distance from a Location in the Baltic Region

Chance of Similarity (%)	Mean Distance (km)	Maximum Distance (km)	Minimum Distance (km)
100	0	0	0
90	5.35	5.56 (66°)	5.1 (-43°)
80	51.38	53.78 (25°)	48.32 (-55°)
66	295.08	>300 (66°)	260.86 (-67)
50	> 300	>300	>300
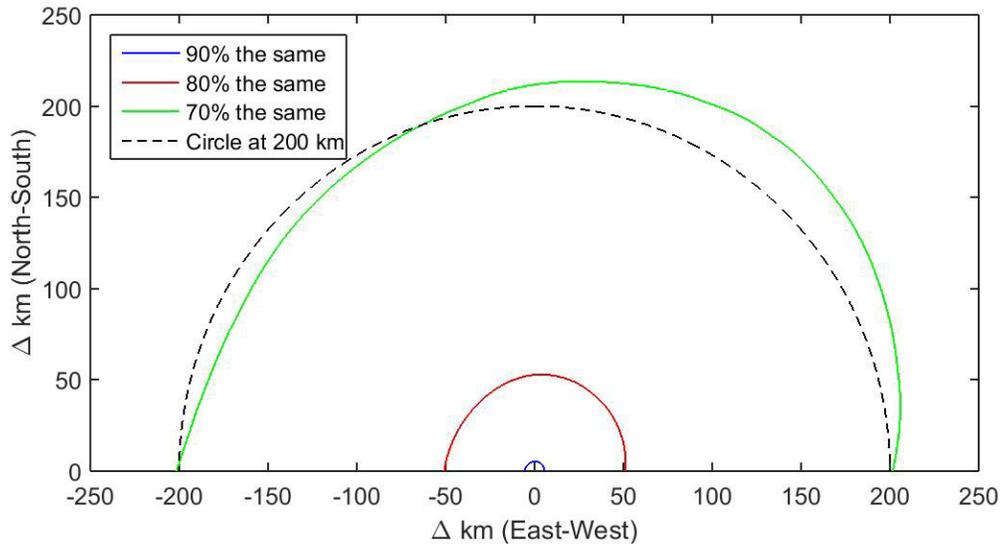
Figure 5-8. Chance of Observing the Same Weather (Cloudy or Clear) a Displaced Distance from a Location in the Baltic Region

Averaging by month reveals great variability in the clustering of clouds by season. Figure 5-8 depicts the average distance (over all directions) for $P_{same} = 90$ percent. For the winter seasons, large stratus coverage (or large open sky) most likely dominates, due to the higher self-similarity of the weather. Smaller, cumulus cloud fields are more common in the spring and summer, increasing the frequency of gaps in the clouds.

4.   Discussion

Based upon the analysis presented in this section, we can reach some general conclusions on cloud cover over the Baltic. As evident in Figure 5-6, the fraction of the

Baltic region covered in clouds varies more significantly within a month than between months, although the winter months tend to be the most cloudy, and the summer months the most clear. Of the 937 pictures of the Baltic, 99.9 percent of the region was covered in clouds on the cloudiest day and only 5.5 percent on the clearest day. We found little spatial variability in the time averaged cloud coverage for the interior land regions of the Baltic region (see Figure 5-9).
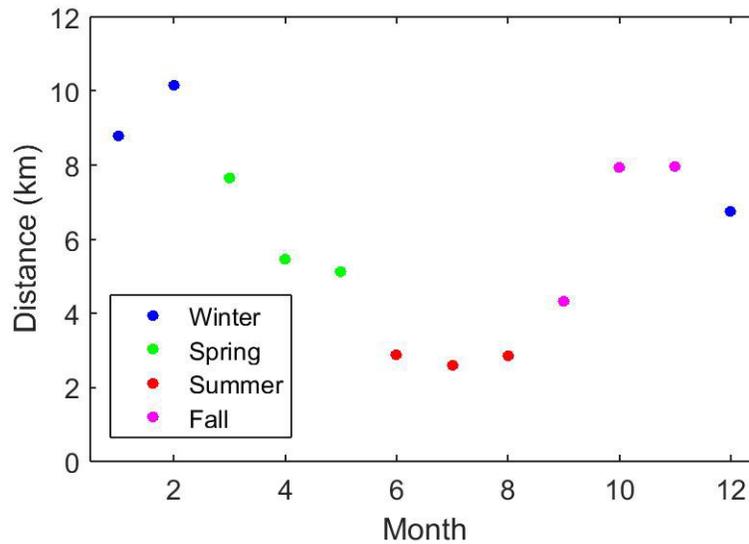
Figure 5-9. Monthly Dependence of Average Distance for P_{same} = 90 Percent
Higher distances correspond to larger cloudy and clear regions.

Using the autocovariance metric, we found that weather (cloudy or clear) in the Baltic region is quite similar on length scales < 10 km. Thus, whether blocked by clouds or with a clear line of sight, one is very likely to be blocked or have clear line of sight (respectively) within distance scales of 10 km away. This result is consistent with the discussion of cloud's horizontal distributions in Section 2.C, namely that the average piece of cloud tends to exist in large clouds over tens of kilometers in length. Cloud occurrence doesn't become statistically dissimilar until distances of hundreds of kilometers away. Winter months have the largest, most uniform cloud fields and summer months have the most variable cloud fields. However, just like the cloud fraction, the spatial correlation of clouds varies significantly between observations in time in a manner probably comparable to the variation in the cloud fraction. We found only weak directional dependence on cloud spatial correlation, with clouds being the most self-similar in the northeastern-southwestern direction.

References

1. Institute for Defense Analyses, *Global Hawk Block 30 Improvements Study: Sensor Integration, Cost, and Effectiveness*, Volume 1, IDA Paper P-5236, 2015, UNCLASSIFIED.

2. Reinke, D. L., "Probability of cloud-free line of sght (PCFLOS) derived from CloudSat cloud profiling radar (CPR) and coincident CALIPSO lidar data," *17th Conference on Satellite Meteorology and Oceanography*, 2010.

3. Lund, I. A. and M. D. Shanklin, "Photogrammetrically determined cloud-free lines-of-sight through the atmosphere," *Journal of Applied Meteorology*, 11(5):773–782, 1972.

4. Killen, R. M. and R. G. Ellingson, "The effect of shape and spatial distribution of cumulus clouds on longwave irradiance," *Journal of the Atmospheric Sciences*, 51(14):2123–2136, 1994.

5. Ma, Yingtao, "Longwave radiative transfer through 3d cloud fields: testing the probability of clear line of sight models with the arm cloud observations" (PhD diss., University of Maryland, College Park, 2004).

6. Shields, J. E., A. R. Burden, R. W. Johnson, M. E. Karr, and J. G. Baker, "Measurement and evaluation of cloud free line of sight with digital whole sky imagers," *The Battlespace Atmospheric and Cloud Impacts on Military Operations (BACIMO) Conference*, 2005.

7. Taylor, P. C. and R. G. Ellingson, "A study of the probability of clear line of sight through single-layer cumulus cloud fields in the tropical western Pacific," *Journal of the Atmospheric Sciences*, 65(11):3497–3512, 2008.

8. Venkat, R. A. and D. W. Young, "Cloud-free line-of-sight estimation for free space optical communications," *Proc. of SPIE*, volume 8732, pages 873205–1, 2013.

9. Mace, G. G. and Q. Zhang, "The CloudSat radar-lidar geometrical profile product (RL-GeoProf): Updates, improvements, and selected results" *Journal of Geophysical Research: Atmospheres*, 119(15):9441–9462, 2014.

10. Trebbin, Nico, "Cloud Statistics from Calipso Lidar Data for the Performance Assessment of a Methane Space Lidar," (PhD diss., TU München, 2013).

11. Sassen K., Z. Wang, and D. Liu, "Global distribution of cirrus clouds from CloudSat/Cloud-Aerosol lidar and infrared pathfinder satellite observations (CALIPSO) measurements," *Journal of Geophysical Research: Atmospheres*, 113(D8), 2008.

12. Wood, R. and P. R. Field, "The distribution of cloud horizontal sizes" *Journal of Climate*, 24(18):4800–4816, 2011.

13. Institute for Defense Analyses, *Development of the IDA Sensing Effectiveness Evaluator (ISEE) Model for Airborne Intelligence, Surveillance, and Reconnaissance*, IDA Paper P-4771, 2011, UNCLASSIFIED.

14. Rossow, W. B., C. Delo, and B. Cairns, "Implications of the observed mesoscale variations of clouds for the Earth's radiation budget" *Journal of Climate*, 15(6):557–585, 2002.

15. Ackerman S., K. Strabala, P. Menzel, R. Frey, C. Moeller, and L. Gumley, "Discriminating clear-sky from cloud with MODIS algorithm theoretical basis document (MOD35)," *MODIS Cloud Mask Team, Cooperative Institute for Meteorological Satellite Studies, University of Wisconsin*. Citeseer, 2010.

(This page is intentionally blank.)

6.   Conclusion and Path Forward

This report details three case studies utilizing global, open-source, scientific datasets of cloud occurrences. Although not specifically designed for remote-sensing applications, these datasets provide high-quality measurements of the earth's atmosphere anywhere on the globe. In characterizing the typical cloud coverage that a geographical location may have in a particular season in a particular scenario, we can estimate the extent to which clouds may preclude remote sensing over the EO/IR portion of the electromagnetic spectrum.

Well known to the scientific community are the technical limitations to satellite retrievals of clouds' optical properties. Satellite observations do not provide measurement of a cloud's optical and physical properties with quality as high as in situ measurements via aircraft or balloon. For example, CloudSat's calculations of optical depth, liquid water content, and cloud type are based upon models derived from in situ measurements and are inferences rather than measurements. However, by using the results of a peer-reviewed detection algorithm for each data source, we can confidently estimate how often clouds of some threshold thickness occur at a particular location.

The scientific satellite datasets of CloudSat/CALIOP and MODIS provide measurements of the earth's atmosphere on a global scale. However, because of the resolution limitations of these datasets, one cannot get images of scattered or broken cloud decks as detailed as those provided by aircraft or ground observations, such as whole sky imagers [1, 2]. Considering the general opacity of clouds, the preponderance of large, connected cloudy regions, and our work analyzing the CloudSat/CALIOP and MODIS datasets, the angular dependence of PCFLOS is not a factor as critical for remote-sensing applications as altitude, geographical location, or season. (Of course, given a particular cloudy field, it could be an important factor.) In addition, we found that the resolution limitations of these datasets can be a benefit because the limited resolution makes the datasets smaller and more tractable for our purposes.

Our team has a few potential modeling directions in which we could go to improve upon our ability to assess the frequency of cloud blockages for remote-sensing applications. The scientific datasets used in this report are derived from sun-synchronous satellite observations and provide only a snapshot of where the clouds were, not how they move. Numerical weather prediction models such as the Weather Research and Forecasting Model (WRF) can provide estimates of how clouds move and develop in time, but these models require significant computational power and expertise to operate. Indeed, the question of how clouds evolve in time is much more complicated than the dynamics of a wind field. Potentially we could use the statistics of cloud persistence developed by Lund and Shanklin in 1972 [3]. We are hopeful that we can extract more information through parametric studies with known, simple

assumptions rather than through more complicated, higher fidelity models with intractable assumptions.

An additional path of work would be merging the datasets of MODIS and CloudSat/CALIOP. MODIS's CloudMask product places clouds on a plane of the earth's surface without information on height; CloudSat and CALIOP provide a trace through this plane, profiling cloud height. These pictures are complementary, but they provide an incomplete picture of clouds over a full 3D region of the earth. Statistics of spatial correlations of the clouds can be calculated easily within each dataset (see Section 5.C). With further assumptions (such as clouds being isotropic in the earth's plane), we might be able to construct a reasonable 3D cloud field based upon these observations. In so doing, the cloud-blockage calculation in ISEE would become an explicit line-of-sight calculation from the observer to the target. However, the technical challenges of constructing a reasonable 3D cloud field and the calculation of LOS through a 3D latitude, longitude, and elevation grid are daunting. Less ambitious efforts, such as correlating metrics like average cloud height and average cloud spacing, could be fruitful in future studies.

References

1. Shields, J. E., A. R. Burden, R. W. Johnson, M. E. Karr, and J. G. Baker, "Measurement and evaluation of cloud free line of sight with digital whole sky imagers," *The Battlespace Atmospheric and Cloud Impacts on Military Operations (BACIMO) Conference*, 2005.

2. Taylor, P. C. and R. G. Ellingson, "A study of the probability of clear line of sight through single-layer cumulus cloud fields in the tropical western Pacific," *Journal of the Atmospheric Sciences*, 65(11):3497–3512, 2008.

3. Lund, I. A. and M. D. Shanklin, "Photogrammetrically determined cloud-free lines-of-sight through the atmosphere," *Journal of Applied Meteorology*, 11(5):773– 782, 1972.

Appendix A
Algorithm for Calculating CFLOS in 2D Grid

This section details the algorithm we designed to calculate PCFLOS based upon a series of two-dimensional cloud grids. The software used in the analysis was written using MATLAB; design decisions of the algorithm reflect the strengths of this coding platform.

Consider the following objects as inputs. Define a particular target location T, with a well-defined longitude and latitude. Consider a set of two-dimensional, cloud-fraction grids $CF_{i,j}$, with the column index i of these grids denoting distance along the surface of the earth, and the row index j denoting height relative to sea level. These grids correspond to unique satellite orbits. The grid has regular spacing, 240 meters in the vertical and 1,096 meters in the horizontal; each index i is associated with the same distance regardless of j, but the heights for each column are shifted slightly, with a consistent pattern; thus the heights are nearly unique for each pair i, and j. Each index i is also associated with a longitude and latitude and an elevation G_i, which denotes the elevation of the ground. The values of $CF_{i,j}$ are between 0 and 1.

Now consider a square grid, with roughly the same dimensions as the cloud fractions. The target is identified as the lower, center of the grid, corresponding to the origin with respect to horizontal distance and height (not elevation). A set of observers are placed in the grid, directly above and to the left of the target. Each observer is associated with a height H_{obs} and an angle of observation θ_{obs}. A line of sight is constructed between each observer and the target. Both the grid boxes, which the line of sight transverses, and the length of the line located in each grid box are calculated. As such, each observer is associated with a set of indices and lengths in the square grid, which will be used for the PCFLOS calculation to follow. (We note that this step of the algorithm was the most difficult to design but resulted in a tremendous speed-up in calculation)

The main calculation of PCFLOS starts by looping through a set of two-dimensional cloud grids CF_{ij}. If the minimum distance of the satellite's ground path is less than some critical distance (we selected 25 km), the cloud fraction matrix is fed into the PCFLOS algorithm. This algorithm begins by associating $CF_{i,j}$ with a square grid. Since the actual heights of each vertical column shift slightly, this procedure has a maximum error of 120 meters in the vertical direction. Next, looping through observers, PCFLOS is calculated for each observer using the following formula:

$$\text{PCFLOS}_{\text{obs}} = \prod_k \left(1 - \text{CF}_{i(k),j(k)}\right)^{L(k)/h} \tag{A-1}$$

Here k denotes the index in the set of grid boxes that a line of sight between the observer and the target crosses through. The indices $i(k)$ and $j(k)$ denote the location in the square

grid of the indices, and $L(k)$ denotes the length of the line in the box. The length is normalized by the characteristic length h, which we took to be the height of each grid box, 240 meters.

Equation A-1 relies upon the interpretation that the chance of clear line of sight to the target is the product of the probabilities of seeing through each grid box in between. Since the cloud fractions $CF_{i,j}$ are primarily zeros and ones, practically every box between the target and the observer must be clear of clouds. However, in the event that a box is partially filled with clouds, the probability of seeing through the clouds partially filling one box is independent of the probability of seeing through another box. The form of the exponent and normalization factor h was chosen in keeping with this interpretation; if the observer is directly above the target, the chance of seeing through a partially cloudy grid box is taken to be $1 - CF$, in keeping with the definition of cloud fraction (see Section 3.B). As a consequence of the exponent, a line of sight that travels through a grid box diagonally with a length twice the height of the grid is treated as two separate grid boxes with identical cloud fraction and an independent probability of being blocked by clouds.

Upon completing the calculation of PCFLOS for each observer, the resulting vector is stored as a column in a matrix, with an index n. Since this index is associated with a particular orbit of the satellite, any dependency of PCFLOS on time covered in the dataset can be extracted. For example, by averaging PCFLOS with respect to n over all orbits in December, January, and February, we can estimate the chance of cloud-free line of sight the observers might have in winter.

Appendix B
Using Autocovariance to Measure
the Spatial Correlation of Clouds

Autocovariance and autocorrelation are linked concepts and are used interchangeably in some contexts. The autocovariance can be calculated in a continuous form on any function or in a discrete form on an array of values. Here, we will be using the discrete form of autocovariance, using the common definition of autocovariance as a truncated estimator:

$$ACov_{\Delta i, \Delta i} = \frac{1}{(N-\Delta i)(M-\Delta j)} \sum_{i=1}^{N-\Delta i} \sum_{j=1}^{M-\Delta j} \left(CF_{ij} CF_{i+\Delta i, j+\Delta j} \right) \qquad \text{(B-1)}$$

The autocovariance $ACov_{\Delta i, \Delta i}$ is a matrix, defined with respect to non-negative change in index Δi in the eastern direction, and non-negative change in index Δj in the northern direction. Since our matrix of clouds CF are defined on a regularly spaced grid, these changes in indices correspond to changes in distances. Because of the edges of the domain, the autocovariance is defined from a distance of zero to the domain length. The autocovariance is termed "truncated" since the indices only extend to the edge of the grid and do not wrap around to the other side as in a circular domain. Thus, locations in the center of the Baltic region are going to more heavily influence the autocovariance calculation, since they will be compared with locations to their left and their right (or top and bottom), but locations at the edges will only be compared with those in the direction nearer to the center.

To quickly calculate autocovariance, we used an equivalent definition to Eq. B-1, defined using discrete Fourier transforms. This definition uses zero padding to temporarily increase the size of the domain [1]. Many common definitions for autocovariance normalize the target function or array by its mean. We did not normalize for reasons that will be discussed in the following paragraphs.

To help clarify the following discussion, we will use the subscript notation to identify the indices of a matrix and a superscript to describe the object. For example, $ACov\Delta i, \Delta j$ denotes the value of matrix $ACov$ at indices $\Delta i, \Delta j$.

Equation B-1 calculates the average of a product of two terms: the presence of clouds at one location versus the presence of clouds at a displaced location. Four separate events could occur; index pair i, j and $i + \Delta i, j + \Delta j$ could each be cloudy or clear. For each pair of displacement lengths $\Delta i, \Delta j$, define the number of occurrences for each of the four cases

as $K_{C,C}$, $K_{C,O}$, $K_{O,C}$, and $K_{O,O}$, with C denoting clouds and O denoting clear sky. In addition, associate each number of occurrence with an observed likelihood P, where,

$$P \equiv K / (N - \Delta i)(M - \Delta j)$$ (B-2)

(Note we have dropped the superscript denoting displacement length for brevity). The above equation defines the probability of an event as the frequency of occurrences over the total number of occurrences. One of these four results must occur for each pair calculated in Eq. B-1, and thus,

$$P_{C,C} + P_{C,O} + P_{O,C} + P_{O,O} = 1$$ (B-3)

Finding the probability P for each of the four cases is our goal in determining the local spatial correlation of clouds. However, using an algorithm to go through the matrix, and count $K_{C,C}$, $K_{C,O}$, $K_{O,C}$, and $K_{O,O}$ for each pair of displacement lengths would be tootime consuming, and a limiting factor for matrices of this size. (Four indices must be iterated through to compare locations in a 2D matrix). However, we can use the autocovariance, defined using Fourier transforms and calculated using the fast-Fourier transform algorithm, to vastly speed up the calculation.

By defining our cloud fraction matrix CF to be equal to 1 given the presence of clouds and equal to 0 given the absence of clouds, the product of two locations will be zero if any of the two locations is clear, and one if they are both cloudy. Thus only both clouds being present yield a value of 1 in the double sum of Eq. B-1, and $ACov = P_{C,C}$. Using Eq. B-3, we have $1 - ACov = P_{C,O} + P_{O,C} + P_{O,O}$; we cannot distinguish the cases of no clouds being present from both cloudy and clear.

To distinguish between those cases, define a new cloud fraction matrix CF^* equal to 1 when clouds are present and -1 instead of 0 when clouds are not present. If only one of the locations is covered in clouds, the product will yield -1. The autocovariance will be an average of the two cases. It follows that $ACov^* = 2P_{same} - 1$, and $P_{diff} = (1 - ACov^*)/2$, where $P_{same} = P_{C,C} + P_{O,O}$ and $P_{diff} = P_{C,O} + P_{O,C}$.

Combining the equations from both cloud fraction matrices, we have,

$$P_{C,C} = ACov$$ (B-4)

$$P_{C,O} + P_{O,C} + P_{O,O} = 1 - ACov$$ (B-5)

$$2P_{C,C} + 2P_{O,O} = 1 + ACov^*$$ (B-6)

$$P_{C,O} + P_{O,C} = (1 - ACov^*)/2$$ (B-7)

where $ACov$ and $ACov^*$ are known. Solving the system of equations yields,

$$P_{O,O} = 1/2 - ACov + ACov^*/2$$ (B-8)

$$P_{C,O} + P_{O,C} = {(1 - ACov^*)}/{2} \qquad \text{(B-9)}$$

Here, each equation holds for each pair of displacement lengths Δi, Δj. Since multiplication is associative, we cannot distinguish $P_{O,C}$ from $P_{C,O}$, and there is no motivation to do so in this study.

To summarize, we can use the autocorrelation function to calculate the frequency of concurrent cloud coverage over the Baltic. This frequency is calculated for a single cloud scene, and can be averaged over an ensemble of cloud scenes.

Strictly speaking, cloud occurrence over the Baltic is not a second-order stationary process; the autocovariance might vary with respect to space and time. If we were to separate the Baltic into four smaller regions, the resulting autocovariances would be different for each. For this analysis, we average over the entire region and over time.

Reference

1. Nion T., "Autocorrelation functions," http://www.tibonihoo.net/literate_musing/autocorrelations.html, 2012, accessed: 2016-04-10.

(This page is intentionally blank.)

Appendix C
List of Illustrations

Figures

Tables

Appendix D
Bibliography

Ackerman S., K. Strabala, P. Menzel, R. Frey, C. Moeller, and L. Gumley, "Discriminating clear-sky from cloud with MODIS algorithm theoretical basis document (MOD35)," *MODIS Cloud Mask Team, Cooperative Institute for Meteorological Satellite Studies, University of Wisconsin*. Citeseer, 2010.

Ackerman, S. A., et al., "Retrieval of effective microphysical properties of clouds: A wave cloud case study," *Geophysical Research Letters* 25.8: 1121-1124, 1998.

Beals, M. J., J. P. Fugal, R. A. Shaw, J. Lu, S. M. Spuler, and J. L. Stith, "Holographic measurements of inhomogeneous cloud mixing at the centimeter scale" *Science*, 350(6256):87–90, 2015.

Cowley, Les, "Water Droplets," accessed: 2016-04-5.

Craig F Bohren and Donald R Huffman. *Absorption and Scattering of Light by Small Particles*. John Wiley and Sons Inc., 1983.

Glasstone, Samuel and Philip J. Dolan, eds., *The Effects of Nuclear Weapons*, Washington, DC: Government Printing Office, United States Department of Defense and the Energy Research and Development Administration.

Institute for Defense Analyses, *Cloud-free Line-of-sight (CFLOS) Availability*, IDA Paper P-2655, 1992, UNCLASSIFIED.

Institute for Defense Analyses, *Development of the IDA Sensing Effectiveness Evaluator (ISEE) Model for Airborne Intelligence, Surveillance, and Reconnaissance*, IDA Paper P-4771, 2011, UNCLASSIFIED.

Institute for Defense Analyses, *Estimates of Probability of a Cloud-free Line-of-sight for Raptor Talon*, IDA Paper D-1442, 1994, UNCLASSIFIED.

Institute for Defense Analyses, *Global Hawk Block 30 Improvements Study: Sensor Integration, Cost, and Effectiveness: Volume 1*, IDA Paper P-5236, 2015, UNCLASSIFIED.

Institute for Defense Analyses, *Visual and Infrared Predictor (VIP) Derivations*, IDA Paper D-5397, 2015, UNCLASSIFIED.

Killen, R. M. and R. G. Ellingson, "The effect of shape and spatial distribution of cumulus clouds on longwave irradiance," *Journal of the Atmospheric Sciences*, 51(14):2123–2136, 1994.

Leahy, L.V., R. Wood, R.J. Charlson, C.A. Hostetler, R.R. Rogers, M.A. Vaughan, and D.M. Winker, "On the nature and extent of optically thin marine low clouds," *Journal of Geophysical Research: Atmospheres*, 117(D22), 2012.

Lund, I. A. and M. D. Shanklin, "Photogrammetrically determined cloud-free lines-of-sight through the atmosphere," *Journal of Applied Meteorology*, 11(5):773– 782, 1972.

Ma, Yingtao, "Longwave radiative transfer through 3d cloud fields: testing the probability of clear line of sight models with the arm cloud observations" (PhD diss., University of Maryland, College Park, 2004).

Mace, G. G. and Q. Zhang, "The CloudSat radar-lidar geometrical profile product (RL-GeoProf): Updates, improvements, and selected results" *Journal of Geophysical Research: Atmospheres*, 119(15):9441–9462, 2014.

Mace, G.G., Y. Zhang, S. Platnick, M. D. King, P. Minnis, and P. Yang, "Evaluation of cirrus cloud properties derived from MODIS data using cloud properties derived from ground-based observations collected at the ARM SGP site," *Journal of Applied Meteorology*, 44(2):221–240, 2005.

Marchand, R., G. G. Mace, T. Ackerman, and G. Stephens, "Hydrometeor detection using CloudSat-An Earth-orbiting 94-GHz cloud radar," *Journal of Atmospheric and Oceanic Technology*, 25(4):519–533, 2008.

Nion T., "Autocorrelation functions" http://www.tibonihoo.net/literate_musing/autocorrelations.html, 2012, accessed: 2016-04-10.

RAND, Chen, C.C., Attenuation of Electromagnetic Radiation by Haze, Fog, Clouds, and Rain, R-1 694-PR, 1975.

Reinke, D.L., "Probability of cloud-free line of sght (PCFLOS) derived from CloudSat cloud profiling radar (CPR) and coincident CALIPSO lidar data," *17th Conference on Satellite Meteorology and Oceanography*, 2010.

Rossow, W. B., C. Delo, and B. Cairns, "Implications of the observed mesoscale variations of clouds for the Earth's radiation budget" *Journal of Climate*, 15(6):557–585, 2002.

Sassen K.,Z. Wang, and D. Liu, "Global distribution of cirrus clouds from CloudSat/Cloud-Aerosol lidar and infrared pathfinder satellite observations (CALIPSO) measurements," *Journal of Geophysical Research: Atmospheres*, 113(D8), 2008.

Shields, J. E., A. R. Burden, R. W. Johnson, M. E. Karr, and J. G. Baker, "Measurement and evaluation of cloud free line of sight with digital whole sky imagers," *The Battlespace Atmospheric and Cloud Impacts on Military Operations (BACIMO) Conference*, 2005.

Smith, F. G., J. S. Accetta, and D. L. Shumaker, eds., *The Infrared & Electro-Optical Systems Handbook*; Volume 2, *Atmospheric Propagation of Radiation*, Smith, F. G., ed., Ann Arbor, MI: Infrared Information Analysis Center Environmental Research Institute of Michigan and Bellingham, WA: SPIE Optical Engineering Press, 1993.

Stephens, G. L., D. G. Vane, R. J. Boain, G. G. Mace, K. Sassen, Z. Wang, A. J. Illingworth, E. J. O'Connor, W. B. Rossow, S. L. Durden, et al, "The CloudSat mission and the A-Train: A new dimension of space-based observations of clouds and precipitation," *Bulletin of the American Meteorological Society*, 83(12):1771–1790, 2002.

Stubenrauch, C.J., W.B. Rossow, S. Kinne, S. Ackerman, G. Cesana, H. Chepfer, L. Di Girolamo, B. Getzewich, A. Guignard, A. Heidinger, et al., "Assessment of global cloud datasets from satellites: Project and database initiated by the GEWEX radiation panel," *Bulletin of the American Meteorological Society*, 94(7):1031–1049, 2013.

Tanelli, S., S. L. Durden, E. Im, K. S. Pak, D. G. Reinke, P. Partain, J. M. Haynes, and R. T. Marchand, "CloudSat's cloud profiling radar after two years in orbit: Performance, calibration, and processing," *IEEE Transactions on Geoscience and Remote Sensing*, 46(11):3560–3573, 2008.

Taylor, P. C. and R. G. Ellingson, "A study of the probability of clear line of sight through single-layer cumulus cloud fields in the tropical western Pacific," *Journal of the Atmospheric Sciences*, 65(11):3497–3512, 2008.

Trebbin, Nico, "Cloud Statistics from Calipso Lidar Data for the Performance Assessment of a Methane Space Lidar," (PhD diss., TU München, 2013).

van de Hulst, Hendrik C., *Light Scattering by Small Particles*. New York: John Wiley and Sons Inc., 1957.

Venkat, R. A. and D. W. Young, "Cloud-free line-of-sight estimation for free space optical communications," *Proc. of SPIE*, volume 8732, pages 873205–1, 2013.

Wallace, John M. and Peter V Hobbs, *Atmospheric Science: an Introductory Survey*, volume 92, Academic Press, 2006.

Wang, Pao, *Physics and Dynamics of Clouds and Precipitation*, Cambridge: Cambridge University Press, 2013.

Wood, R. and P. R. Field, "The distribution of cloud horizontal sizes" *Journal of Climate*, 24(18):4800–4816, 2011.

(This page is intentionally blank.)

Appendix E
Acronyms and Abbreviations

Ac	altocumulus
As	altostratus
CALIOP	cloud-aerosol lidar with orthogonal polarization
CAPE	Cost Assessment and Program Evaluation
CF	cloud fraction
CFLOS	cloud-free line-of-sight
CPR	Cloud Profiling Radar
Cu	cumulus
EO	electro-optical
IDA	Institute for Defense Analyses
IR	infrared
ISEE	IDA Sensing Effectiveness Evaluator
lidar	light detection and ranging
MODIS	Moderate Resolution Imaging Spectroradiometer
NASA	National Aeronautical and Space Administration
Ns	nimbostratus
PCFLOS	probability of cloud-free line of sight
Sc	stratocumulus
St	stratus
WRF	Weather Research and Forecasting

(This page is intentionally blank.)

REPORT DOCUMENTATION PAGE

1. REPORT DATE (DD-MM-YY)	2. REPORT TYPE	3. DATES COVERED (FROM – TO)
October 2016	Final	January 2016 – September 2016

4. TITLE AND SUBTITLE

Assessment of Cloud Occurrence and Impact on Remote Sensing using Global, Open-source, Scientific Datasets (REDACTED)

5A. CONTRACT NO.

HQ0034-14-D-0001

5B. GRANT NO.

5C. PROGRAM ELEMENT NO(S).

6. AUTHOR(S)

Slawik, A. J.; Adelizzi, E. A.; Koretsky, G. M.

5D. PROJECT NO.

5E. TASK NO.

CRP C-1300

5F. WORK UNIT NO.

7. PERFORMING ORGANIZATION NAME(S) AND ADDRESS(ES)

Institute for Defense Analyses
4850 Mark Center Drive
Alexandria, VA 22311-1882

8. PERFORMING ORGANIZATION REPORT NO.

IDA Document D-8175- (REVISED)

9. SPONSORING / MONITORING AGENCY NAME(S) AND ADDRESS(ES)

N/A

10. SPONSOR'S / MONITOR'S ACRONYM(S)

11. SPONSOR'S / MONITOR'S REPORT NO(S).

12. DISTRIBUTION / AVAILABILITY STATEMENT

Approved for public release; distribution is unlimited.

13. SUPPLEMENTARY NOTES

Geoffrey M. Koretsky, Project Leader

14. ABSTRACT

This document discusses the prevalence of natural cloud blockages and their seasonal variations in a number of widely dispersed locations. The analysis leverages historical observations data from open sources, including three-dimensional cloud-profiling radar from CloudSat, a Colorado State project, and NASA's Cloud-Aerosol LIDAR with Orthogonal Polarization (CALIOP), and a two-dimensional cloud profile produced by NASA's Moderate Resolution Imaging Spectroradiometer (MODIS), known as CloudMask. The data are used to estimate probabilities of cloud-free line-of-sight (PCFLOS), which are incorporated into an IDA intelligence, surveillance, and reconnaissance (ISR) model. Spatial correlations are also examined.

15. SUBJECT TERMS

Cloud; Intelligence; Surveillance; Reconnaissance; Modeling;

16. SECURITY CLASSIFICATION OF:			17. LIMITATION OF ABSTRACT	18. NO. OF PAGES	19A. NAME OF RESPONSIBLE PERSON
			Unlimited	66	Geoffrey Koretsky
A. REPORT	**B. ABSTRACT**	**C. THIS PAGE**			**19B. TELEPHONE NUMBER (INCLUDE AREA CODE)**
UNCLASSIFIED	UNCLASSIFIED	UNCLASSIFIED			703-845-2455